无辐射跃迁理论进展

牛英利[1*†] 林至闿[2‡] 杨 玲[3] 于建国[4] 何荣幸[5]
庞 然[6] 朱超原[2*§] 林倫年[7] 林聖賢[2§]
(1. 中国科学院化学研究所有机固体重点实验室 北京 100190;
2. 西北大学现代物理研究所 西安 710069;
3. 哈尔滨工业大学基础与交叉科学研究院理论与模拟化学研究所 哈尔滨 150080;
4. 北京师范大学化学学院 北京 100875; 5. 西南大学化学化工学院 重庆 400715;
6. 厦门大学化学化工学院固体表面物理化学国家重点实验室 厦门 361005;
7. 东北大学理学院化学系 仙台 980 日本)

摘 要 在本文中,我们将介绍运用第一性原理计算包含非谐效应或势能面锥形交叉情况下内转换速率的最新工作。我们同时计算了包含非谐效应的分子吸收和发射光谱,以检验量子化学方法计算得到势能面的准确性。势能面的锥形交叉对内转换过程的影响是学界广泛关注的焦点。本文将介绍如何在内转换速率计算的过程中考虑势能面锥形交叉的影响,并将之运用于吡嗪分子。本文运用绝热近似理论处理了另外一个重要的无辐射过程,分子的振动弛豫过程,并将这个理论应用于水二聚体和苯胺的振动弛豫速率的计算。

关键词 无辐射跃迁 内转换 振动弛豫 双井势 非谐效应
中图分类号: O643.3; TQ51 **文献标识码:** A **文章编号:** 1005-281X(2012)06-0928-22

Recent Developments in Radiationless Transitions

Niu Yingli[1*†] *Lin Chinkai*[2‡] *Yang Ling*[3] *Yu Jianguo*[4] *He Rongxing*[5]
Pang Ran[6] *Zhu Chaoyuan*[2*§] *Hayashi Michitoshi*[7] *Lin Sheng Hsien*[2§]
(1. Key Laboratory of Organic Solids, Institute of Chemistry, Chinese Academy of Sciences, Beijing 100190, China; 2. Institute of Modern Physics, Northwest University, Xian 710069, China;
3. Institute of Theoretical and Simulation Chemistry, Academy of Fundamental and Interdisciplinary Science, Harbin Institute of Technology, Harbin 150080 China;
4. Department of Chemistry, Beijing Normal University, Beijing 100875, China;
5. College of Chemistry and Chemical Engineering, Southwest University, Chongqing 400715, China;
6. State Key Laboratory of Physical Chemistry of Solid Surfaces, College of Chemistry and Chemical Engineering, Xiamen University, Xiamen 361005, China;
7. Department of Chemistry, Faculty of Science, Tohoku University, Sendai 980, Japan)

Abstract In this paper, we introduce recent works on the mathematical treatments and the first-principle calculations concerning the internal conversion rates for the cases with anharmonic potentials, and conical

收稿: 2012 年 2 月, **收修改稿:** 2012 年 4 月

* Corresponding author e-mail: cyzhu@mail.nctu.edu.tw
† Previous work in Institute of Chemistry
‡ Visiting scientist in Northwest University
§ Visiting professor in Northwest University

intersecting potentials. The simulations of absorption and emission spectra with anharmonic effects are also presented to check the validity of the potential energy surfaces obtained from the quantum chemical calculations. The effect of conical intersection on internal conversion has attracted considerable attention. In this paper a different approach is proposed and applied to pyrazine. Another important non-radiative process, molecular vibrational relaxation, is also treated by applying the adiabatic approximation to the ab initio anharmonic potential energy surfaces. The vibrational relaxation rates in water dimer and aniline are chosen to demonstrate the calculation.

Key words　radiationless transition; internal conversion; vibrational relaxation; double well potential; anharmonic effect

1　Introduction

Radiationless transitions which consist of internal conversion (IC) (spin-allowed process) and intersystem crossing (ISC) (spin-forbidden process) play a very important role in photochemistry, photobiology and photophysics. For convenience of discussion, a simplified Jablonski diagram is shown in Fig. 1, which describes the elementary processes of molecular luminescence.

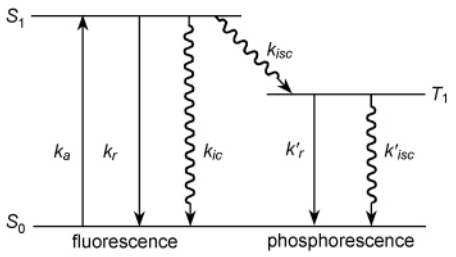

Fig. 1　Elementary photophysical processes of molecular luminescence

$$S_0 + \hbar\omega \xrightarrow{k_a} S_1 \quad \text{absorption} \quad (1.1)$$

$$S_1 \xrightarrow{k_r} S_0 + \hbar\omega' \quad \text{fluorescence} \quad (1.2)$$

$$S_1 \xrightarrow{k_{ic}} S_0 \quad \text{internal conversion} \quad (1.3)$$

$$S_1 \xrightarrow{k_{isc}} T_1 \quad \text{intersystem crossing} \quad (1.4)$$

$$T_1 \xrightarrow{k'_r} S_0 + \hbar\omega'' \quad \text{phosphorescence} \quad (1.5)$$

$$T_1 \xrightarrow{k'_{isc}} S_0 \quad \text{intersystem crossing} \quad (1.6)$$

These elementary processes are the characteristics of a molecule. They determine whether a molecule can be a good candidate for LED or a dye molecule for organic solar cells. In addition, there are two other important elementary processes described in the following.

Photo-induced electron transfer

$$DA \xrightarrow{h\nu} D^* A \rightarrow D^+ A^- \quad (1.7)$$

Photo-induced energy transfer

$$DA \xrightarrow{h\nu} D^* A \rightarrow DA^* \quad (1.8)$$

All the processes involve two electronic states. In other words, they are non-adiabatic in nature. In addition to these processes, there exists another elementary non-radiative process in molecular luminescence, vibrational relaxation (VR), which can take place in either ground or excited electronic states.

In this paper, we will concentrate on recent works concerning the mathematical treatments and the first-principle calculations of the IC and VR processes. A general theory of IC process has been established based on displaced harmonic oscillator approximation (HOA)[1—10]. Mode-mixing effect (Duschinsky rotation effect, DRE)[11] and anharmonic effect are two important effects beyond the HOA. Recently the DRE on radiationless processes for polyatomic molecules has been developed[12—19]. In this paper, we will introduce the works of anharmonic effects of double well and Morse potential energy surfaces (PESs) to the absorption, emission spectra and IC transition. Besides, we will also introduce the Q-dependent method to deal with the IC with conical intersection (CI) of the two relevant PESs. Another non-radiative process, VR, will also be treated by using the anharmonic PES obtained from the quantum chemistry calculations and the adiabatic approximation in this paper.

This paper is organized as follows: Section 2 is about the general formalism of photophysical processes in the framework of Born-Oppenheimer approximation (BOA). Section 3 is the content of applications,

including four parts: Section 3.1 will introduce the calculations of the spectra and the IC rate of formaldehyde, which case has double well PES. Section 3.2 will introduce the formalism and calculations of spectra and the IC rate with anharmonic PES, especially for the Morse potential, in form of the power series. Section 3.3 will introduce the treatment of IC with the effect of CI. Section 3.4 gives the formalism and applications of VR in the adiabatic approximation. And section 4 will give a conclusion in the end.

2 General consideration

All the elementary processes described in Section 1 can be calculated quantum mechanically by using the BOA described in the following

$$\hat{H}\Psi_{av}(q,Q) = E_{av}\Psi_{av}(q,Q) \quad (2.1)$$

$$\Psi_{av}(q,Q) = \Phi_a(q;Q)\,\Theta_{av}(Q) \quad (2.2)$$

$$\hat{H}_e\Phi_a(q;Q) = U_a(Q)\,\Phi_a(q;Q) \quad (2.3)$$

$$(\hat{T}_n + U_a(Q))\,\Theta_{av}(Q) = E_{av}\Theta_{av}(Q) \quad (2.4)$$

where $\hat{H}$ represents the molecular Hamiltonian with the eigenenergy E_{av} and the molecular wavefunction $\Psi_{av}(q, Q)$. $\{q\}$, $\{Q\}$ describe the electronic and nuclear coordinates, respectively. $\Phi_a(q;Q)$ and $\Theta_{av}(Q)$ represent the electronic and nuclear wavefunctions. It should be noted that according to the BOA, the Born-Oppenheimer (BO) states are the molecular eigenstates. If a molecule is in its BO eigenstate, without considering the spontaneous emission, it cannot change its state in BOA. The breakdown of the BOA is due to the non-adiabatic coupling (NAC)

$$\hat{H}'_{\mathrm{BO}}\Phi_a\Theta_{av} = -\frac{\hbar^2}{2}\sum_i\left(2\frac{\partial\Phi_a}{\partial Q_i}\frac{\partial\Theta_{av}}{\partial Q_i} + \frac{\partial^2\Phi_a}{\partial Q_i^2}\right) \quad (2.5)$$

Notice that [12]

$$\left\langle\Phi_b\left|\frac{\partial\Phi_a}{\partial Q_i}\right.\right\rangle = \frac{\left\langle\Phi_b\left|\frac{\partial V}{\partial Q_i}\right|\Phi_a\right\rangle}{U_a(Q) - U_b(Q)} \quad (2.6)$$

Since $U_a(Q)$ and $U_b(Q)$ denote the potential energy surfaces (PESs) of the a and b electronic states, the surface crossing can take place where

$$U_a(Q) = U_b(Q) \quad (2.7)$$

Using the Born-Oppenheimer (BO) wavefunction $\Psi_{av}(q,Q)$ as basis set, we can calculate the rate of IC, ISC, photo-induced energy and electron transfer by using the Fermi golden rule

$$W_{a\to b} = \frac{2\pi}{\hbar}\sum_{v,u}P_{av}|H'_{bu,av}|^2\delta(E_{bu} - E_{av}) \quad (2.8)$$

where P_{av} represents the distribution function, and

$$H'_{bu,av} = \langle\Phi_b\Theta_{bu}|\hat{H}'|\Phi_a\Theta_{av}\rangle = \langle\Theta_{bu}|\hat{H}'_{ba}|\Theta_{av}\rangle \quad (2.9)$$

In Eq. (2.9) $\hat{H}'$ depends on the process under consideration. Similarly for optical absorption, the absorption coefficient can be expressed as

$$\alpha(\omega) = \frac{4\pi^2\omega}{3\hbar c}\sum_{v,u}P_{av}|\vec{\mu}_{bu,av}|^2\delta(\omega_{bu,av} - \omega) \quad (2.10)$$

where $\vec{\mu}_{bu,av}$ denotes the transition dipole moment

$$\vec{\mu}_{bu,av} = \langle\Theta_{bu}|\vec{\mu}_{ba}|\Theta_{av}\rangle \quad (2.11)$$

and for emission spectroscopy, the normalized emission spectrum can be described by

$$I_N(\omega) = \frac{4\omega^3}{3\hbar c^3}\tau_r\sum_{v,u}P_{av}|\vec{\mu}_{bu,av}|^2\delta(\omega_{bu,av} - \omega) \quad (2.12)$$

where τ_r represents the radiative lifetime

$$\tau_r^{-1} = \frac{4}{3\hbar c^3}\sum_{v,u}\omega_{bu,av}^3P_{av}|\vec{\mu}_{bu,av}|^2 \quad (2.13)$$

Next we consider IC process. In the BOA, when the molecule is excited to the excited electronic state a, it will stay in a. Due to the NAC, the BOA breaks down, and the IC rate can be written as

$$W_{a\to b} = \frac{2\pi}{\hbar}\sum_{v,u}P_{av}|\langle\Psi_{bu}|\hat{H}'_{\mathrm{BO}}|\Psi_{av}\rangle|^2\delta(E_{bu} - E_{av}) \quad (2.14)$$

where

$$\langle\Psi_{bu}|\hat{H}'_{\mathrm{BO}}|\Psi_{av}\rangle = \langle\Phi_b\Theta_{bu}|\hat{H}'_{\mathrm{BO}}\Phi_a\Theta_{av}\rangle = -\hbar^2\sum_i\left\langle\Theta_{bu}\left|\left\langle\Phi_b\left|\frac{\partial\Phi_a}{\partial Q_i}\right.\right\rangle\right|\frac{\partial\Theta_{av}}{\partial Q_i}\right\rangle \quad (2.15)$$

Considering the relation of Eq. (2.6), NAC will be singular at the crossing point where $U_a = U_b$. However, due to the anharmonic effect for most molecules, U_{S_0} and U_{S_1} will never cross. However, for higher excited electronic states like S_2, S_3, …, the potential surfaces often cross and conical intersections are believed to play an important role in IC process. Its

treatment will be presented in section 3. 3.

3 Applications

In this section, we will present the recent results of the first-principle calculations of the photophysical properties and processes of various molecules.

3. 1 Formaldehyde

3. 1. 1 Equilibrium structures and the out-of-plane bending mode

The S_0 ($^1A_1$) → S_1 ($^1A_2$) n-π^* transition of formaldehyde has long attracted much interest [20—29]. This symmetry-forbidden transition in the C_{2v} point group could occur through vibronic coupling. Among the six vibrational modes, the only b_1 mode, the out-of-plane bending mode (v_4) plays the leading role by intensity borrowing from a higher $^1B_2$ electronic state that results in the so-called type-B transition bands [20, 24]. The two b_2 vibrational modes (v_5 and v_6), on the other hand, generate the type-C bands by associating with a $^1B_1$ state, and might contribute up to 25% of the observed total absorption intensity [20, 23, 24].

The ground state has a planar geometry at equilibrium. By exciting the electron from the non-bonding orbital of the oxygen atom to the anti-bonding π^* orbital, the equilibrium structure of the S_1 state distorts to a pyramid (C_s point group) [23, 26, 27]. The out-of-plane bending vibrational mode is quite anharmonic, essentially possessing a symmetric double-well potential. A schematic diagram illustrating the potential surfaces of the out-of-plane bending mode is given in Fig. 2, and the major transitions and couplings between the ground and the excited states are shown as well.

Lin et al [30] have carried out several first-principle computational approaches including MP2, CASSCF, and DFT with the B3LYP functional to figure out the equilibrium structures and energies of these states, summarized in Table 1 and Table 2. It was found that all vibrational modes keep the harmonicity upon excitation to the S_1 state, except the out-of-plane bending mode (v_4).

For this particular double-well mode, it has been proved that an empirical three-parameter formula

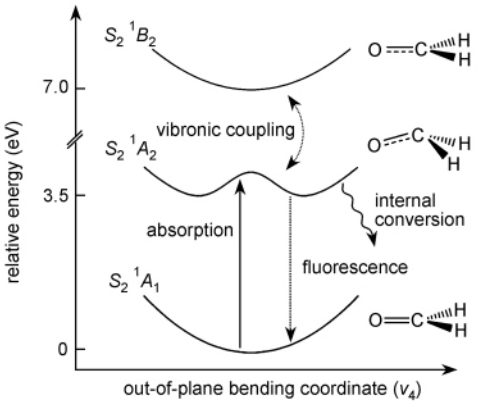

Fig. 2 A schematic diagram showing the ground and the first two singlet excited state potentials of formaldehyde along the out-of-plane bending mode (not on scale), demonstrating the double-well character of the S_1 state. The equilibrium structures as well as the major transitions are also illustrated.

Table 1 Equilibrium structures and vibrational frequencies of the ground state S_0($^1A_1$) of formaldehyde

	expt. [a]	MP2	CAS(8,16)	CAS(12,14)	B3LYP
geometric parameters					
r_{CO}(Å)	1. 207	1. 213	1. 209	1. 211	1. 201
r_{CH}(Å)	1. 117	1. 105	1. 101	1. 119	1. 109
a_{OCH}(°)	121. 9	121. 9	121. 9	122. 0	122. 0
a_{HCH}(°)	116. 2	116. 1	116. 1	116. 0	115. 9
vibrational frequencies (cm^{-1}) [b]					
v_1	2 783 (2 978)	2 975	3 018	2 842	2 882
v_2	1 746 (1 778)	1 761	1 805	1 774	1 817
v_3	1 500 (1 529)	1 559	1 619	1 530	1 532
v_4	1 167 (1 191)	1 207	1 268	1 189	1 203
v_5	2 843 (2 997)	3 047	3 084	2 904	2 939
v_6	1 249 (1 299)	1 278	1 334	1 265	1 260

[a] ref [28]

[b] Experimental fundamental frequencies from ref [28] and harmonized frequencies (in parentheses) from ref [29] are shown.

proposed by Coon et al. could elegantly reproduce the measured data [31].

$$V(Q) = \frac{1}{2}\omega_0^2 Q^2 + A\exp(-\alpha Q^2) \quad (3.1)$$

Lin et al [30] solved the vibrational energy levels variationally with their own algorithm, and described the wavefunction of each level as a linear combination

of harmonic oscillator wavefunctions of the unperturbed fundamental angular frequency. The fitting parameters, energy levels and Franck-Condon integrals are listed in Table 3.

Table 2 Equilibrium structures, vibrational frequencies and excitation energies of the first singlet excited state $S_1(^1A_2)$ of formaldehyde

	expt.[a]	CAS(8,16)	CAS(12,14)
excitation energies (eV)			
$\Delta E_{vertical}$	3.94	4.13	4.23
$\Delta E_{adiabatic}$	3.50	3.43	3.84
geometric parameters			
r_{CO}(Å)	1.323	1.348	1.350
r_{CH}(Å)	1.098	1.089	1.108
a_{OCH}(°)	115.1	113.8	114.4
a_{HCH}(°)	118.4	119.1	117.8
$\theta_{out\text{-}of\text{-}plane}$(°)	34.0	37.2	36.8
vibrational frequencies (cm^{-1})			
v_1	2 847	3 079	2 916
v_2	1 173	1 170	1 145
v_3	1 290	1 393	1 351
v_4	*[b]	708	738
v_5	2 968	2 664	3 020
v_6	904	587	961

[a] refs [23] and [28]

[b] highly anharmonic

Table 3 Potential parameters and vibrational energy levels of the out-of-plane bending mode for the S_1 state and the Franck-Condon integrals between S_0 and S_1 states of formaldehyde

potential parameters[a]

ω_0 (2π cm^{-1})	A (cm^{-1})	α ($2\pi\omega_0/\hbar$)	ρ	B (cm^{-1})	$G(0)$ (cm^{-1})
688.9	3 952.0	0.1437	0.50	356.5	239.0

vibrational energy levels

u	0	1	2	3	4
calc. (cm^{-1})	0.0	124.6	542.3	948.0	1 425.9
expt. (cm^{-1})[b]	0.0	124.6	542.3	947.9	1 429.3

Franck-Condon overlap integrals[c]

$v\backslash u$	0	1	2	3	4
0	0.7157	0.0000	−0.6361	0.0000	0.2660
1	0.0000	0.6406	0.0000	−0.6388	0.0000
2	0.5385	0.0000	0.2643	0.0000	−0.5986

[a] $\rho \equiv \ln(2\alpha A/\omega_0^2)$, B is the barrier-height parameter, and $G(0)$ is the zero-point energy. All parameters are defined in ref [30]

[b] ref [21]

[c] v and u refer to vibrational quantum numbers of v_4 of S_0 and S_1 states, respectively

3.1.2 Absorption spectrum

The $S_1(^1A_2) \leftarrow S_0(^1A_1)$ absorption transition of formaldehyde is forbidden by the symmetries of adiabatic electronic wavefunctions and electric transition dipoles in the C_{2v} point group, $\vec{\mu}_{10}^0 = \langle\Phi_1^0|\vec{\mu}|\Phi_0^0\rangle = 0$ (see eqs. (2.10) and (2.12)). However this transition is vibronically allowed. Theoretically it can be regarded as intensity borrowing through vibronic coupling with other electronic states [32,33].

There are three possible inducing modes whose vibrational quantum number change from $v_i = 0$ to odd u_i; the transition with $i = 4$ is classified as type-B, while that with $i = 5$ or 6 is type-C [24]. The remaining three totally symmetric modes, v_1 to v_3, could play as the progressing mode.

Regarding the experimental absorption spectra, there are three main progressions induced by v_4 (4_0^1 and 4_0^3) and v_5 (5_0^1). v_2 is the major progressing mode, v_1 participates as a minor one, and v_3 is invisible. The third possible inducing mode, v_6, is not individually assigned [23,24,28]. The contribution of each progressing mode can be analyzed by considering the Huang-Rhys factor [34]. The values of 0.60, 2.40 and 0.04 were obtained for the three totally symmetric modes by CAS (12,12). Hence we could expect that the v_2 progression maximizes at $u_2 = 2$ and 3, performing the most obvious peak series; the v_1 progression shows the most probable transition to $u_1 = 0$ or 1, and the v_3 one should keep its vibrational quantum number at 0. In addition, the relative intensities of peaks in each progression series are proportional to their Franck-Condon factors, which in term relate to Huang-Rhys factors and vibrational quantum numbers. The $4_0^3/4_0^1$ band head intensity ratio was therefore predicted as 0.99. In principle there is a third band head, 4_0^5, which has the expected intensity ratio $4_0^5/4_0^1$ to be about 0.35, but this peak and the related progressions have never been assigned. It might be attributed to the large-amplitude out-of-plane bending motion which yields a dissociative potential at high vibrational quanta, resulting in shift of peak positions and drastic reduction of vibrational overlap integrals.

The relative intensities between progressions of different inducing modes depend not only on the vibrational overlap (Franck-Condon) part but also on the electronic part determined by vibronic-coupled transition dipole moments and frequencies. The ratio of

band head intensities of different inducing modes was then calculated as $5_0^1/4_0^1 = 0.56$ and $6_0^1/4_0^1 = 0.13$. It turned out that the progression induced by v_5 and v_6 takes ~ 21% and ~ 5% of the total absorption intensity, respectively, consistent with a previous suggestion that type-C transitions take 25% of the total oscillator strength [20]. The relative intensities of v_5 and v_6 progressions are also reasonable, since in experimental absorption spectra the latter makes relatively small contribution [26].

Fig. 3 illustrates the simulated absorption spectrum considering v_2, v_4 and v_5 based on the CAS (12,14) calculation. The magnitude of the Franck-Condon factor is marked under each absorption peak. In the low-frequency (long-wavelength, 300—360 nm) region where the peak broadening and the anharmonic effect are not severe, the simulated spectrum shows rather good consistence with the experimental report [26].

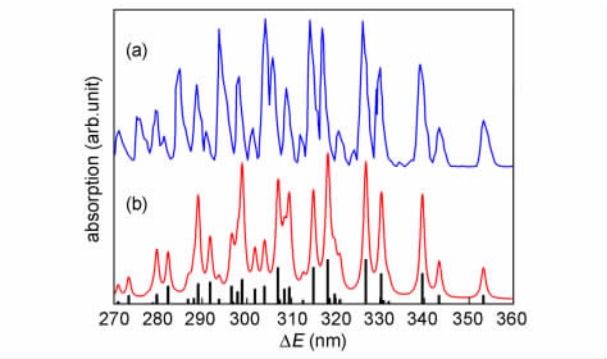

Fig. 3 Absorption spectra of the $S_1\,^1A_2 \leftarrow S_0\,^1A_1$ transition of formaldehyde. (a) Experimental data adopted from ref [26]. (b) Simulated results by CAS(12,14) with the vertical bars indicating Franck-Condon factors of each vibronic transition

3.1.3 Radiative and non-radiative transition rate constants

The excitation is followed by several possible relaxation processes: fluorescence emission, internal conversion, intersystem crossing, dissociation and/or collisional energy transfer. The radiative lifetime was found to be several μs, and the non-radiative one several tens ns from the lowest vibrational levels of the S_1 state [24, 35—37].

The fluorescence emission could be treated in a similar vibronic-coupling manner to the absorption transition. On the other hand, the internal conversion is provided by the breakdown of the BOA through the nuclear kinetic energy operator (see eqs. (2.14) and (2.15)) [1, 32, 38].

The transition rate constants of the $S_1 \rightarrow S_0$ radiative and non-radiative relaxation pathways are shown in Table 4. Fluorescence emission is the only radiative process directly originated from the S_1 state, and the rate constant is determined by the vibronic-coupled dipole terms. The calculated data predicted the radiative lifetime values around 9 to 15 μs depending on the choice of the active space and states averaged in CASSCF, which are roughly consistent to the experimentally recorded 3.3 μs [24].

Table 4 Radiative and non-radiative transition rate constants (W) and lifetime (τ) of the $S_1 \rightarrow S_0$ relaxation of formaldehyde[a]

	CASSCF				expt.[b]
	11-SA[c]		17-SA		
radiative transition					
W_r (s^{-1})	1.09×10^5		6.47×10^4		3.03×10^5
τ_r (μs)	9.2		15.5		3.3
non-radiative transition					
	CASSCF (Lorentzian)[d]		CASSCF (saddle point)		expt.
	11-SA	17-SA	11-SA	17-SA	
W_{nr} (s^{-1})	1.21×10^7	3.79×10^6	3.47×10^7	2.15×10^7	1.18×10^7
τ_{nr} (ns)	83	264	29	47	85

[a] from the lowest vibrational level of the excited state

[b] ref [24]

[c] number of states averaged in CASSCF

[d] with a fixed dephasing constant $\gamma = 150 \times 2\pi$ cm^{-1}

For the non-radiative processes, IC is regarded as the only important channel since the coupling between $S_1(^1A_2)$ and $T_1(^3A_2)$ is quite weak and the lifetime of ISC is much longer [24, 39, 40], and unimolecular dissociation does not occur directly from the excited state potential energy surface but from the highly excited vibrational levels of the ground state after internal conversion [35, 38]. Once the BO coupling terms were obtained by collecting calculated vibronic-coupling coefficients, vibrational frequencies and Franck-Condon overlap integrals, the total transition rate constant of IC was estimated by two approaches: (a) summation of rate constants of single vibronic

levels with assumed dephasing constants in Lorentzian lineshape functions; (b) integration using the saddle point method. In the former approach, the major difficulty was that first-principle calculations could not provide any information of dephasing constants. The upper limit of the dephasing constant was evaluated as $\gamma = 150 \times 2\pi$ cm^{-1} from peak widths in experimental absorption and/or emission spectra[26], and this value was adopted for all single-vibronic-level transitions for simplicity. Compared with experimentally measured non-radiative lifetime of ~ 85 ns from the lowest vibrational level of the excited state, the 11-state-averaged calculation obtained quite a good value while the 17-state-averaged result made somewhat overestimation. Note that the real dephasing typically enlarges as the vibrational quantum number increases, and the calculated rate constant of a single vibronic level will further raise if this factor is taking into account.

Within the saddle point method, the problem of undetermined dephasing constant was technically avoided. It was noticed that in generating nuclear correlation functions, some additional approximations concerning displaced and distorted oscillators have also been taken into account. This method estimated a lifetime around 30 to 50 ns which was in good agreement with the experimental one[24].

It turns out that both treatments yielded rather consistent values with reasonable assumptions on the dephasing constants and in the mathematical derivations. The correctness of predicted transition rate constants then depended considerably on the computation of vibronic coupling coefficients. The higher accuracy could be achieved, in principle, by (a) increasing the number of excited states to an extent where the contribution from even higher states converges due to the increase of energy gap, and by (b) enlarging the active space for a more appropriate description on the potential energy surfaces, that is, toward the full configuration interaction. The investigations with the 17-state-averaged CAS(8,18) calculations have moderately approached this extent. A more detailed derivation of mathematical frameworks and analysis of calculated results can be found in ref [41].

3.2 Anharmonic effect on elementary photophysical processes

3.2.1 General formalism

Apply the first-order anharmonic correction to HOA. Starting with perturbation expansion of the jth vibrational normal-mode potential as[42]

$$V_j(Q) = a_{j2}Q_j^2 + \lambda a_{j3}Q_j^3 + \lambda^2 a_{j4}Q_j^4 + \cdots \quad (3.2)$$

in which λ is chosen as a perturbation parameter and Q_j is mass-weighted normal-mode coordinate. It should be noted that, $V_j(Q)$ can be Morse potential function:

$$V_j(Q) = D_j(1 - e^{-a_jQ_j})^2 \quad (3.3)$$

then

$$a_{j2} = D_j a_j^2, \quad \lambda a_{j3} = -D_j a_j^3, \quad \lambda^2 a_{j4} = \frac{7}{12}D_j a_j^4 \quad (3.4)$$

The energy level and wavefunction for vibrational normal mode v_j can be expanded as a power series,

$$\varepsilon_{v_j} = \varepsilon_{v_j}^{(0)} + \lambda\varepsilon_{v_j}^{(1)} + \lambda^2\varepsilon_{v_j}^{(2)} + \cdots \quad (3.5)$$

and

$$\chi_{v_j}(Q_j) = \chi_{v_j}^{(0)}(Q_j) + \lambda\chi_{v_j}^{(1)}(Q_j) + \lambda^2\chi_{v_j}^{(2)}(Q_j) + \cdots \quad (3.6)$$

where $\chi_{v_j}^{(0)}(Q_j)$ denotes the harmonic wavefunction. Following Appendix A of ref [42], we have the energy levels up to the second-order as

$$\varepsilon_{v_j}^{(0)} = \hbar\omega_j\left(v_j + \frac{1}{2}\right) \quad (3.7)$$

$$\varepsilon_{v_j}^{(1)} = 0 \quad (3.8)$$

and

$$\varepsilon_{v_j}^{(2)} = \hbar\chi_{jj}^0 + \hbar\chi_{jj}\left(v_j + \frac{1}{2}\right)^2 \quad (3.9)$$

in which

$$\hbar\chi_{jj}^0 = \frac{3}{2}a_{j4}\left(\frac{\hbar}{2\omega_j}\right)^2 - \frac{7a_{j3}^2}{2\hbar\omega_j}\left(\frac{\hbar}{2\omega_j}\right)^3 \quad (3.10)$$

and

$$\hbar\chi_{jj} = 6a_{j4}\left(\frac{\hbar}{2\omega_j}\right)^2 - \frac{30a_{j3}^2}{\hbar\omega_j}\left(\frac{\hbar}{2\omega_j}\right)^3 \quad (3.11)$$

where χ_{jj}^0 and χ_{jj} represent the certain anharmonic constants that are estimated from the diagonal parts of the general form derived from the third and the fourth derivatives with respect to normal-mode coordinates. The wavefunction for the first-order correction is

$$\chi_{v_j}^{(1)}(Q_j) = -\frac{a_{j3}}{\hbar\omega_j}\left(\frac{\hbar}{2\omega_j}\right)^{3/2} \times \{3[\sqrt{(v_j+1)^3}\chi_{v_j+1}^{(0)}(Q_j) - \sqrt{v_j^3}\chi_{v_j-1}^{(0)}(Q_j)] + \frac{1}{3}\sqrt{(v_j+1)(v_j+2)(v_j+3)}\chi_{v_j+3}^{(0)}(Q_j) - \frac{1}{3}\sqrt{v_j(v_j-1)(v_j-2)}\chi_{v_j-3}^{(0)}(Q_j)\} \quad (3.12)$$

The first-order correction is zero for energy but is nonzero for wavefunction. Within the displaced anharmonic oscillator approximation up to the first-order correction, absorption coefficient is analytically derived as [42]

$$\alpha(\omega) = \frac{2\pi\omega}{3\hbar c}|\vec{\mu}_{ba}|^2 \int_{-\infty}^{\infty} dt\, e^{it(\omega_{ba}+\Omega_0-\omega)-\gamma_{ba}|t|} \times \exp\{-\sum_j S_j(1+3\eta_j) \times [2\bar{v}_j + 1 - (\bar{v}_j+1)e^{it\omega_j} - \bar{v}_j e^{-it\omega_j}]\} \quad (3.13)$$

for excitation from electronic ground state a to excited state b that means $\omega_{ba} > 0$ in eq. (3.13) for adiabatic energy gap between b and a. According to the eq. (2.12) the fluorescence coefficient is analytically derived as

$$I(\omega) = \frac{2\omega^3}{3\pi\hbar c^3}\tau_r|\vec{\mu}_{ba}|^2 \times \int_{-\infty}^{\infty} dt\, e^{-it(|\omega_{ba}|+\Omega_0-\omega)-\gamma_{ba}|t|} \times \exp\{-\sum_j S_j(1-3\eta_j) \times [2\bar{v}_j + 1 - (\bar{v}_j+1)e^{it\omega_j} - \bar{v}_j e^{-it\omega_j}]\} \quad (3.14)$$

for transition from electronic excited state a to ground state b that means $\omega_{ba} < 0$ in eq. (3.14) for adiabatic energy gap between b and a. Other quantities are the same for both eqs. (3.13) and (3.14), where $\bar{v}_j = (e^{\hbar\omega_j/k_BT} - 1)^{-1}$ is the average phonon distribution, γ_{ba} represents the dephasing constant (with relation to the lifetime $\tau_{ba} = 1/\gamma_{ba}$) between two electronic states, and $\vec{\mu}_{ba}$ is the electronic transition dipole moment. The most important quantities Ω_0 and η_j stand for the first-order anharmonic correction to Franck-Condon factors and given by

$$\Omega_0 = -2\sum_j \eta_j S_j \omega_j \quad (3.15)$$

and

$$\eta_j = \frac{a_{j3}d_j}{a_{j2}} = \frac{a_{j3}d_j}{0.5\omega_j^2} \quad (3.16)$$

where ω_j is harmonic vibrational normal-mode frequency, and the Huang-Rhys factor S_j, the displacement d_j, the second coefficient a_{j2}, and the third coefficient a_{j3} are defined as

$$S_j = \frac{1}{2\hbar}\omega_j d_j^2 \quad (3.17)$$

and

$$d_j = Q'_j - Q_j = \sum_n L_{jn}(q'_n - q_n) \quad (3.18)$$

$$a_{j2} = \frac{1}{2}\frac{\partial^2 V}{\partial Q_j} = \frac{1}{2}\omega_j^2 \quad (3.19)$$

$$a_{j3} = \frac{1}{3!}\frac{\partial^3 V}{\partial Q_j^3} = \frac{1}{3}K_{j3} \quad (3.20)$$

Inserting eq. (3.20) into eq. (3.16) leads to

$$\eta_j = \frac{2K_{j3}d_j}{3\omega_j^2} = \frac{K_{j3}d_j^3}{3S_j\hbar\omega_j} \quad (3.21)$$

The q'_n and q_n in eq. (3.18) are the mass-weighted Cartesian coordinates at the equilibrium geometries of the electronic excited and ground states, respectively. If the dimensionless first-order anharmonic parameter η_j is equal to zero, the absorption coefficient in eq. (3.13) and fluorescence coefficient in eq. (3.14) are exactly same as displaced harmonic oscillator approximation. An anharmonic parameter η_j in eq. (3.16) is determined by eq. (3.21) where the diagonal element K_{j3} of cubic force constant with respect to normal mode coordinate can be estimated from quantum chemistry program package.

The breaking down of mirror image between absorption and fluorescence spectra is immediate consequence from the first-order anharmonic correction to Franck-Condon factors, in which the effective Huang-Rhys factor $S'_j = (1 \pm 3\eta_j)S_j$ (+ for absorption in eq. (3.13) and − for fluorescence emission in eq. (3.14)) is no longer the same. The profiles of absorption and fluorescence spectra now can be very different in shape as well as in intensity. Another anharmonic effect from the first-order contribution is that the harmonic 0→0 excitation energy is shifted by Ω_0 that is interpreted as a dynamic correction to the main peak of 0→0 transition in spectra.

Although in this part, only the anharmonic effect on absorption and emission spectra has been discussed, it can, however, be applied to study radiationless

transition, electron transfer, energy transfer etc.

3.2.2 Anharmonic Franck-Condon simulation for the excited state $S_1(^1B_1)$ of pyridine

Zhu et al simulated the absorption spectrum and the fluorescence emission spectrum for $S_1(^1B_1)$ state based on both displaced harmonic and displaced anharmonic oscillator approximations at the temperature taken as 298K at which the experimental spectra were obtained [43]. The present anharmonic correction is up to the first-order perturbation to HOA. The main progressions of vibrational bands for the S_1 absorption and fluorescence spectra come from v_{6a} mode accompanied by sub-contributions from modes v_1 and v_{12} modes. The Huang-Rhys factors for the modes v_{6a}, v_1, and v_{12} are 1.41, 0.5 and 0.54, respectively. They produce the main contribution for both absorption spectrum shown in Fig. 4 and fluorescence spectrum shown in Fig. 5 within the observed spectrum band region.

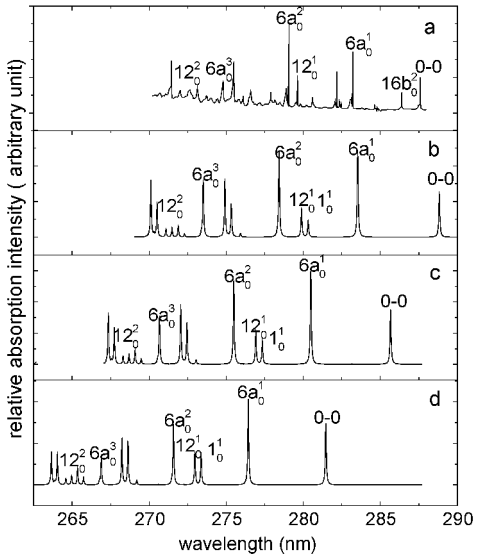

Fig. 4 $S_1(^1B_1) \leftarrow S_0(^1A_1)$ absorption spectrum of pyridine. (a) Experimental data from ref [44]. Spectrum simulated from the present anharmonic correction with (b) $\sqrt{3}\eta_i$ and (c) η_i for all ten totallic symmetric modes. (d) Spectrum simulated from the present HOA

The overall progressions of spectra are reproduced by HOA as shown in Fig. 4d and Fig. 5d. We utilize the best static excitation energy $|\omega_{ab}| = 4.41$ eV from the ab initio calculation so that the peak position of the 0-0 excitation from HOA still shows a big discrepancy with experiment observation. When we add anharmonic correction estimated from B3LYP method, we obtain anharmonic parameters η_i that lead to spectrum shift $\Omega_0 = -523\ \mathrm{cm}^{-1}$ (the minus corresponds to red shift of spectrum). If we introduce scaling scheme that is widely used in harmonic frequency calculation, we change η_i into $\sqrt{3}\eta_i$, and this leads to spectrum shift $\Omega_0 = -\sqrt{3} \times 523\ \mathrm{cm}^{-1}$. This results in the correct peak position for 0-0 transition as well as the other peaks for both absorption and fluorescence spectra.

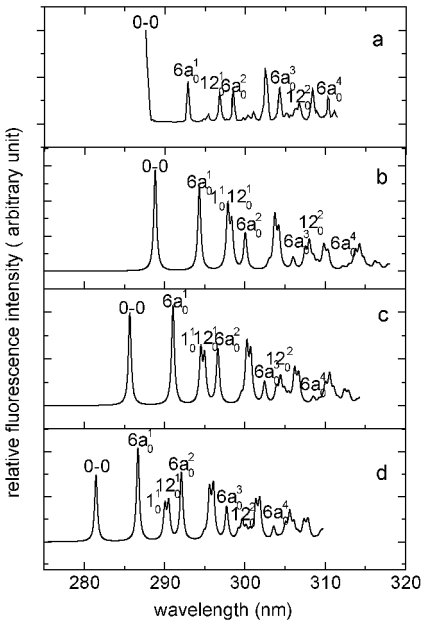

Fig. 5 $S_1(^1B_1) \rightarrow S_0(^1A_1)$ fluorescence spectrum of pyridine. (a) Experimental data from ref [45]. Spectrum simulated from the present anharmonic correction with (b) $\sqrt{3}\eta_i$ and (c) η_i for all ten totally symmetric modes. (d) Spectrum simulated from the present HOA

We conclude that $\Omega_0 = -0.11$ eV is dynamic correction to static adiabatic excitation energy $|\omega_{ab}| = 4.41$ eV. At the same time, the anharmonic quantity $\eta_{6a} = 0.08$ makes effective the Huang-Rhys factor $S'_{6a} = S_{6a}(1 + 3\eta_{6a}) = 1.75$ for absorption and $S'_{6a} = S_{6a}(1 - 3\eta_{6a}) = 1.1$ for fluorescence, and this leads to v_{6a} transition profiles and relative intensity changes as well. The first-order anharmonic correction makes both spectra shift and profile change simultaneously in the right direction in comparison with experimental absorption and fluorescence spectra for S_1

state. All detailed analysis is given in ref [43].

3.2.3 Anharmonic Franck-Condon simulation for the excited state $S_1(^1B_1)$ of pyrimidine

Yang et al [46] utilize the normal-mode frequencies calculated from MP2 method to simulate both absorption and fluorescence spectra for the excited state S_1 ($^1B_1$) within both displaced harmonic and anharmonic oscillator approximations. Temperature is taken as 298 K in the simulation at which the experimental spectra were measured. Fig. 6 and Fig. 7 show that the main progressions of vibronic bands for the absorption and fluorescence spectra that are well described by mode ν_{6a} accompanied with modes ν_1 and ν_{12}. In fact, this can be easily understood from that the Huang-Rhys factors for the modes ν_{6a}, ν_1, and ν_{12} are 1.566, 0.299, and 0.454, respectively. The overall agreement between experimental and the presently simulated spectra is generally good. However, the highest peak is assigned as the 0-0 vibronic transition for the absorption and the $6a_0^1$ transition for fluorescence spectra from experiment, while the $6a_0^1$ is the strongest transition for both the absorption and fluorescence spectra from the present calculation. When the anharmonic quantity $\eta_{6a} = -0.004$ is included, the Huang-Rhys factor for absorption becomes $S'_{6a} = S_{6a}(1 + 3\eta_{6a}) = 1.547$ and for fluorescence, $S'_{6a} = S_{6a}(1 - 3\eta_{6a}) = 1.585$, and the ν_{6a} transition profiles and relative intensity change in the right direction as illustrated in Fig. 6b and Fig. 7b. Fig. 6c and Fig. 7c show that the peak position of the 0-0 excitation from HOA has a big discrepancy with experimental observation although the best static excitation energy $|\omega_{ab}| = 3.75$ eV is chosen for simulation. When anharmonic corrections are included in the simulation, Fig. 6b and Fig. 7b show that the peak position of the 0-0 excitation has blue shift $\Omega_0 = 827$ cm^{-1} with respect to HOA and this leads to a very good agreement with experimental observation.

We conclude that the first-order anharmonic correction makes both spectral position shift and profile change simultaneously in the right direction in comparison with experimental absorption and fluorescence spectra for S_1 state. Finally, we have included the distorted effect for the non-total symmetric

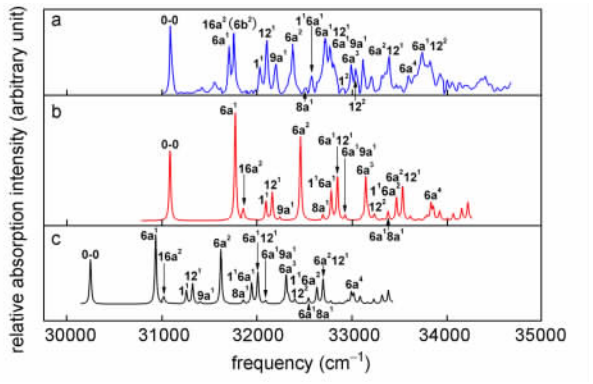

Fig. 6 S_1 ($^1B_1$) ← S_0 ($^1A_1$) absorption spectrum of pyrimidine. (a) Experimental data from ref [47]. (b) Simulated results with the present anharmonic correction. (c) Simulated results with the present HOA

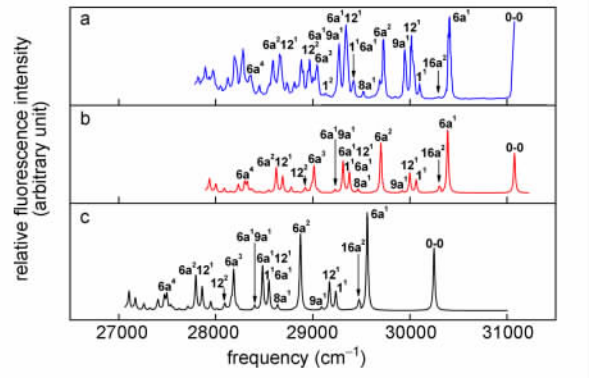

Fig. 7 S_1 ($^1B_1$) → S_0 ($^1A_1$) fluorescence spectrum of pyrimidine. (a) Experimental data from ref [48]. (b) Simulated results with the present anharmonic correction. (c) Simulated results with the present HOA

mode $16a^2$ as is shown in Fig. 6 and Fig. 7 for a very weak band for both the absorption and the fluorescence spectra. All detailed analysis is given in ref [46].

3.2.4 Franck-Condon simulation of the spectrum and radiative and non-radiative rates of fluorobenzene

The simulation of the dispersed fluorescence (DF) spectrum of the $A^1B_2 \rightarrow X^1A_1$ transition for fluorobenzene, and its IC rate and lifetime for this transition will be presented.

3.2.4.1 $A\ ^1B_2 \rightarrow X\ ^1A_1$ dispersed fluorescence spectrum

The dispersed fluorescence (DF) spectrum of the $A^1B_2 \rightarrow X^1A_1$ transition was measured and the detailed analyses were reported in the recent experiment studies [49], where the DF spectral profile is primarily described by the Franck-Condon progression in terms of

the totally symmetric normal modes (a$_1$-type). Among these modes, ν_9 and ν_{10} are the main progression forming modes in the $^1B_2 \rightarrow {}^1A_1$ fluorescence spectrum. The present calculations confirmed that modes ν_{10} and ν_9 have the largest Huang-Rhys factors (S = 0.420 and 0.408 for instance from B3LYP calculation) and are assigned as the closest analogy to the ring-breathing modes in benzene. The modes ν_2, ν_3, ν_4 and ν_5, which are related to the CH stretching and bending vibrations, have little contribution to Franck-Condon factor as their Huang-Rhys factors are negligibly small. Furthermore, there exist very weak bands in DF spectrum, most of which are related to the non-totally symmetric normal modes, e. g. ν_{19} and ν_{16} (b_1 symmetry), that can be interpreted in terms of Duschinsky mixing. In the present spectra simulation, the band origin (0-0 transition) is set up to be zero (cm^{-1}) in the DF spectrum as it was adopted in experimental study [48]. The DF spectrum simulated from B3LYP, B3LYP-35, BHandHLYP, and CIS methods all show that the 0-0 transition is the strongest transition in the allowed $^1B_2 \rightarrow {}^1A_1$ electronic transition as shown in Fig. 8 and Fig. 9, and this agrees with experimental observation. All simulated DF spectra in Fig. 8 and Fig. 9 were performed in the framework of displaced harmonic and anharmonic oscillator approximation, respectively, in which the most prominent peaks have been assigned based on the present calculations in comparison with experimental data. It can be seen that all methods including CIS reproduce qualitatively the essential character of the observed spectrum.

The mode ν_9 displays very strong intensity in the spectral profile as shown in B3LYP calculation in which the intensity of the vibronic line assigned as 9_1^0 fundamental is slightly underestimated; the intensity of 9_1^0 transition in experiment is about 70% of that of the 0-0 line, but that in the present calculation is about 50%. Harmonic Franck-Condon simulations in Fig. 8 all indicate that the strongest and second strongest vibronic transitions are the 10_1^0 and 9_1^0 (after the 0-0 transition) which seems to be reversed in comparison with the experimental result. When anharmonic corrections are added, simulations in Fig. 9 from all

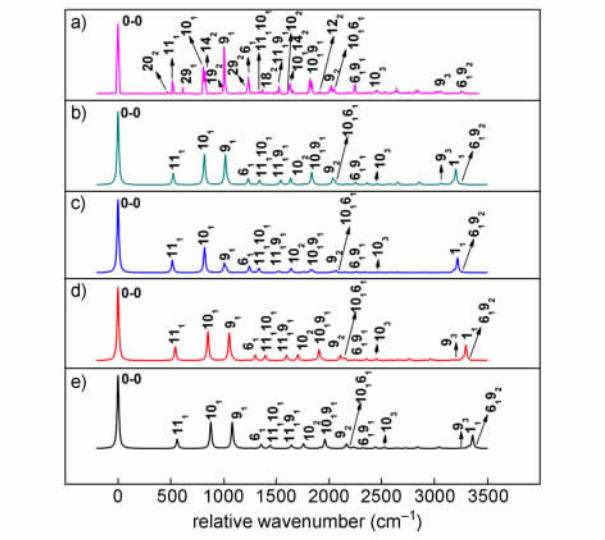

Fig. 8 The DF spectra of fluorobenzene from S_1 to S_0 transition calculated by harmonic FC simulation (the relative energy of the 0-0 transition is set up to be zero). (a) Experimental result from ref [49], (b) (TD) B3LYP, (c) (TD) B3LYP-35, (d) (TD) BHandHLYP and (e) HF/CIS calculations [49]

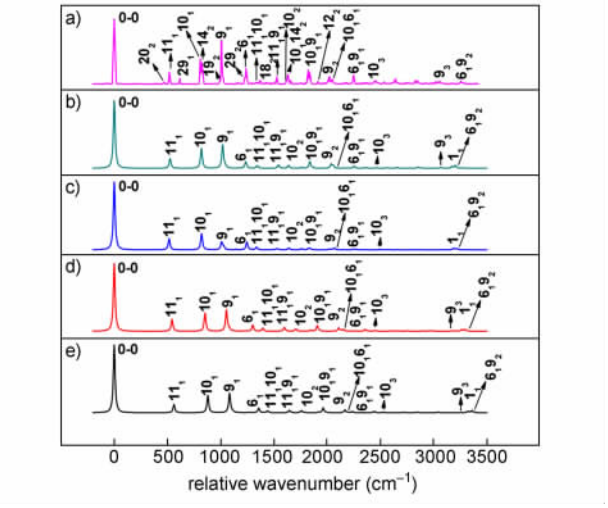

Fig. 9 The same as Fig. 8 but including anharmonic corrections

methods except B3LYP-35 show that the 9_1^0 band is stronger than 10_1^0 band in good agreement with experimental observation. Moreover, harmonic Franck-Condon simulations in Fig. 8 all indicate that there is a strong peak in high energy region of DF spectra and this corresponds to the 1_1^0 transition. When anharmonic corrections are added, simulations in Fig. 9 from all methods show that 1_1^0 transition is diminished. This is because that the Huang-Rhys factor 0.22 for mode ν_1 is

significantly reduced with anharmonic correction. Within the harmonic approximation vibrational displacement vector for mode v_1 (CH stretching) is very large and even if CH bond lengths change very little from S_0 to S_1 state, Huang-Rhys factor is still as big as 0.22. However, anharmonic correction is also large and it effectively cancels out the 1_1^0 transition. We can conclude that the amount of HF exchange (20% in B3LYP, 35% in B3LYP-35, 50% in BHandHLYP, and 100% in HF) does impact the geometries and vibrational frequencies of FB molecule, but not the relative intensities of the transitions. It is anharmonic corrections that influence the relative intensities of the transitions. The experimental spectra in Fig. 8a and Fig. 9a show that the 10_1^0 transition strongly overlaps with 14_2^0 transition with a just split of 15 cm^{-1}. According to the calculations based on the non-totally symmetric vibrational transitions, it is found that the 14_2^0 should be about one-third of the 10_1^0 in transition intensity. It should be also noticed that in the present simulation, the 10_2^0 transition and the combination band $10_1^0 14_2^0$ are nearly degenerate vibronic level pairs; the vibrational origins of 10_2^0 ($2v_{10}$ = 1 637 cm^{-1}) and $10_1^0 14_2^0$ ($v_{10} + 2v_{14}$ = 1 613 cm^{-1}) are separated by 24 cm^{-1} from B3LYP calculation. This suggests that there should be strong coupling between these two vibronic transitions (v_1 and v_{14}). On the other hand, from B3LYP calculation as shown in Fig. 8b and Fig. 9b we could assign the 10_2^0 (1 637 cm^{-1}, that is, $2v_{10}$), 10_3^0 (2 456 cm^{-1}), 9_2^0 (2 036 cm^{-1}) and 9_3^0 (3 054 cm^{-1}) vibronic transitions as four fundamentals located at 1 613, 2 434, 2 016 and 3 014 cm^{-1} in experiment, respectively. The detailed assignments based on the present analysis are shown in very good agreement with the experimental data. In the low energy region of DF spectrum, the experimental observation and the present B3LYP simulation agree well for the significant intensity assigned from the normal mode v_{11}, and this corresponds to the Huang-Rhys factor S = 0.154 (from B3LYP). Intensity of 6_1^0 band in the harmonic Franck-Condon simulation is lower than the corresponding experimental intensity, but it is improved with anharmonic correction as shown in Fig. 9. This fundamental v_6 corresponds to the CF bond stretching in the present analysis. Fig. 8a and Fig. 9b demonstrate how good agreement is for DF spectrum between the experimental result and the present B3LYP simulation in terms of the ordering and positioning of these combination peaks as well as its intensity strengths, especially for extremely weak peak of the combination band of $9_2^0 6_1^0$ in the high frequency region which is also reproduced correctly.

3.2.4.2 Internal conversion rate and the lifetime of S_1 state

Since we are interested in the IC rate constant from the single vibronic level iv produced by the pumping laser, in the Condon and the displaced harmonic oscillator approximations under the collision-free condition, it can be expressed as [50]

$$k_{iv\to f} = \frac{1}{\hbar^2} |R_l(fi)|^2 \int_{-\infty}^{\infty} dt \prod_k g_{v_k}(t) \times \exp\left[it(\omega_{fi} + \omega_l) - \gamma_{if}|t| - \sum_j S_j(1 - e^{it\omega_j}) \right] \quad (3.22)$$

where

$$g_{v_k}(t) = \sum_{n_k=0}^{v_k} \frac{v_k!}{(v_k - n_k)!(n_k!)^2} \times \left[S_k\left(e^{\frac{it\omega_k}{2}} - e^{-\frac{it\omega_k}{2}}\right)^2 \right]^{n_k} \quad (3.23)$$

In the present work, we only consider $v_k = 0$, and thus $g_{v_k}(t) = 1$. $R_l(fi)$ in eq. (3.22) denotes the vibronic coupling for single prompting mode l between the initial and final electronic states and is given by

$$R_l(fi) = -\hbar^2 \sqrt{\frac{\omega_l}{2\hbar}} \langle \Phi_f | \partial/\partial Q_l | \Phi_i \rangle \quad (3.24)$$

where vibronic couplings $\langle \Phi_f | \partial/\partial Q_l | \Phi_i \rangle$ (between S_0 and S_1 states) is defined vertically at equilibrium geometry of S_1 state. At the equilibrium geometry of the S_1 state calculated by two methods: (TD) B3LYP and HF/CIS, we employed CASSCF method for calculating nonadiabatic coupling matrix elements. We should mention that the equilibrium geometry optimized by (TD) B3LYP and HF/CIS methods may or may not correspond to true equilibrium optimized by CASSCF method, but on the other hand, vibronic couplings vary very slowly against the change of geometry. We first computed vibronic couplings in Cartesian coordinate spaces and then transformed them into normal mode

coordinates. However, we have to lower the group symmetry to C_1 in order to perform vibronic couplings by Molpro[51]. We obtained 30 vibronic couplings among which there are only three modes at the same order of magnitude and the rest of them are negligibly small. These three modes do not have clear correspondence to modes obtained with C_{2v} group symmetry. Therefore, we can only label them according to order of frequency magnitude in C_1 symmetry, and they are 7th, 8th and 15th vibrational normal modes computed by CASSCF. Then, three vibronic couplings are converted to the electronic part of the IC rate $|R_l(fi)|^2/\hbar^2$ by eq. (3.24) and the results are given in Table 5.

Table 5 The coupling matrix elements and electronic part of the IC rate of three dominant promoting modes. The Mulliken notation is used to denote the vibrational mode

mode	sym.	TD(B3LYP)		HF/CIS	
		$\langle\Phi_f\|\partial/\partial Q_l\|\Phi_i\rangle$ (a.u.)	$\|R_l(fi)\|^2/\hbar^2$ ($\times10^{15}$ cm^{-1}/s)	$\langle\Phi_f\|\partial/\partial Q_l\|\Phi_i\rangle$ (a.u.)	$\|R_l(fi)\|^2/\hbar^2$ ($\times10^{15}$ cm^{-1}/s)
7th	*a*	0.1482	1.1996	0.1460	0.9352
8th	*a*	0.1324	3.4187	0.1284	2.6908
15th	*a*	0.1054	2.8348	0.1035	2.3069

Two methods produce almost the same coupling matrix elements and its electronic parts of the IC rate (see the coupling elements of the 7th normal mode about 0.1482 and 0.1460 au., respectively from (TD) B3LYP and HF/CIS methods given in Table 5). This is because the optimized geometries of the excited state S_1 performed by the two methods show only small discrepancies, besides the fact that vibronic couplings vary slowly against change of geometry.

Now we turn to compute the second part of IC rate of the transition $^1B_2\rightarrow{}^1A_1$, and that is the integral part in eq. (3.22). The dephasing width γ_{if} in eq. (3.22) is chosen as four values: 5 cm^{-1}, 10 cm^{-1}, 15 cm^{-1} and 20 cm^{-1}, so that calculated IC rate $k_{iv\rightarrow f}$ (or lifetime $\tau_l = 1/k_{iv\rightarrow f}(l)$) for single promoting mode l is a function of dephasing widths. Then, we can estimate total lifetime as

$$\tau_T = \frac{1}{\sum_l k_{iv\rightarrow f}(l)} = \frac{1}{\sum_l (1/\tau_l)} \qquad (3.25)$$

where summation is over three promoting modes (7th, 8th and 15th in the C_1 group symmetry). All results are given in Table 6.

Table 6 The evaluated IC rate (k_{iv}) and lifetime (τ_l) for each of three promoting modes as well as the total lifetime (τ_T) for the $^1B_2\rightarrow{}^1A_1$ transition against different dephasing widths

γ(cm^{-1})	mode	TD(B3LYP)			HF/CIS[a]			exp.[a]
		k_{iv} (10^7 s^{-1})	τ_l (ns)	τ_T (ns)	k_{iv} (10^7 s^{-1})	τ_l (ns)	τ_T (ns)	τ_T (ns)
5	7th	0.65	154	21	0.50	200	44	14.75 ± 0.34
	8th	2.33	43		0.85	118		
	15th	1.69	59		0.94	106		
10	7th	1.48	68	11	0.84	119	19	
	8th	4.23	24		2.42	41		
	15th	3.54	28		2.10	48		
15	7th	2.21	45	7.3	1.26	79	12	
	8th	6.34	16		3.64	27		
	15th	5.31	19		3.15	32		
20	7th	2.95	34	5.4	1.68	60	9.3	
	8th	8.45	12		4.85	21		
	15th	7.08	14		4.20	24		

[a] ref [49]

Table 6 shows that calculated IC rate constants (the lifetimes) increase (decrease) with the increase of the dephasing width for each of the three promoting modes. For example, the TD(B3LYP) calculation indicates that the IC rate constant of mode 8th increases from 2.33×10^7 s^{-1} to 4.23×10^7 s^{-1} when

dephasing width increases from 5 cm^{-1} to 10 cm^{-1}. It should be emphasized that the electronic part of IC rate $|R_l(fi)|^2/\hbar^2$ is independent of dephasing width, and thus it is nuclear part of IC rate that is depending on dephasing width. How to determine dephasing width seems becoming a problem. If we use the consistent choice of dephasing width for both calculations of DF spectrum and IC rate, we should choose the dephasing width as 10 cm^{-1} that was used for the DF spectrum simulation. At γ_{if} = 10 cm^{-1} the calculated total lifetime of the decay $^1B_2 \rightarrow {}^1A_1$ are 11 ns and 19 ns, respectively from TD (B3LYP) and HF/CIS calculations in comparison with the experimental value 14.75 ± 0.34 ns [52] (the lifetime of 0-0 deexciting transition is considered so that $g_{v_k}(t)$ = 1 in eq. (3.22)). The present calculations show a very good agreement with experiment for the IC rate constant (or decay lifetime). Taking both the approximations introduced in the present calculations and the experimental uncertainties into consideration, we conclude that the difference between the calculated and the experimental lifetime (or the IC rates) is quite reasonable. We added anharmonic corrections to the second part of IC rate, and the results are the same as harmonic approximation. All detailed analysis is given in ref [53].

3.3　Internal conversion with conical intersection

CIs play a crucial role in the photophysics and photochemistry of most polyatomic molecules. The effects of CI on IC have been much discussed and numerous CI PESs have been obtained [54, 55]. In this section we will introduce the theoretical treatment of IC process with CI using the case of pyrazine (see Fig. 10).

Recently, the pump-probe experiment for studying the ultrafast dynamics $S_2(\pi\pi^*) \rightarrow S_1(n\pi^*)$ of pyrazine has been carried out by Suzuki et al [57]. Employing the 22 fs duration lasers, they obtained the lifetime for pyrazine as $\tau(S_2)$ = 22 ± 2 fs. This result is in agreement with previous theoretical dynamic simulation [58] and calculation in diabatic representation [19]. In this paper we propose new treatment of IC with CI, especially including Q-dependent non-adiabatic coupling. This model can be

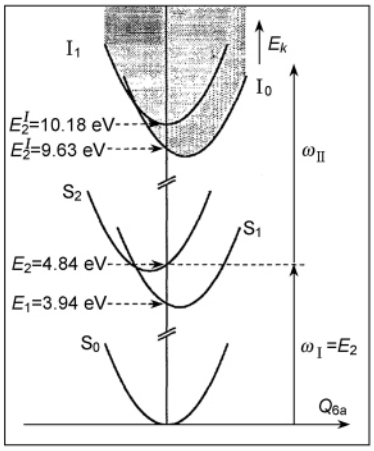

Fig. 10　A cut through the PESs of pyrazine along the normal coordinate Q_{6a} from ref [56]. The vertical energy differences and shifts are drawn on scale. The shaded areas symbolize the ionization continua. The arrows on the right hand side indicate a possible two photon transition

commonly used to describe the CI of any two electronic states of an organic molecule. Near the bottom of the two PESs, the two electronic states in the "diabatic" approximation are described by Φ_1^d ($n\pi^*$) and Φ_2^d ($\pi\pi^*$). The adiabatic approximation Φ_1^{ad} and Φ_2^{ad} will be employed to describe the electronic states around the CI region. Thus

$$\Phi_1^d = \cos\theta\ \Phi_1^{ad} + \sin\theta\ \Phi_2^{ad} \qquad (3.26)$$

and

$$\Phi_2^d = -\sin\theta\ \Phi_1^{ad} + \cos\theta\ \Phi_2^{ad} \qquad (3.27)$$

The adiabatic potential energy surfaces of Φ_1^{ad} and Φ_2^{ad} are given by [55]

$$U_1 = \frac{(H_{11} + H_{22}) + [(H_{11} - H_{22})^2 + 4H_{12}^2]^{\frac{1}{2}}}{2} \qquad (3.28)$$

and

$$U_2 = \frac{(H_{11} + H_{22}) - [(H_{11} - H_{22})^2 + 4H_{12}^2]^{\frac{1}{2}}}{2} \qquad (3.29)$$

where

$$\tan 2\theta = \frac{2H_{12}}{H_{11} - H_{22}} \qquad (3.30)$$

Here, the H_{ij} (i, j = 1, 2) are the Hamiltonian matrix elements in the diabatic representation. To analyze the non-adiabatic dynamic data of pyrazine reported by Suzuki et al [57] and to use the PESs of Domcke et al [56], we use the dimensionless normal coordinate

$$Q_j = \sqrt{\frac{\omega_j}{\hbar}} \sum_i L_{ij} M_i^{\frac{1}{2}} q_i \qquad (3.31)$$

where ω_j is the angular frequency of the jth mode. L_{ij} represents the element of eigenvector matrix of Hessian matrix. q_i is the cartesian coordinate, and M_i is the corresponding nuclear mass, respectively. We then apply the linear coupling approximation [55]

$$H_{11} - H_{22} = \bar{\kappa}(Q_t - \bar{Q}_t), \quad H_{12} = \bar{\lambda} Q_c \qquad (3.32)$$

where Q_t and Q_c denote the totally symmetric mode (that is, an accepting mode, or tuning mode), and the vibronic coupling mode (that is, the promoting mode), respectively. The point $(Q_t, Q_c) = (\bar{Q}_t, 0)$ is just the crossing point of the $\pi\pi^*$ and $n\pi^*$ PESs (i. e. $U_1 = U_2$). Notice that

$$(H_{11} - H_{22})^2 + 4H_{12}^2 = \bar{\kappa}^2 (Q_t - \bar{Q}_t)^2 + 4\bar{\lambda}^2 Q_c^2 \qquad (3.33)$$

At the points other than $(Q_t, Q_c) = (\bar{Q}_t, 0)$, U_1 and U_2 represent conical surfaces.

The IC rate for the electronic transition $a \rightarrow b$ based on the breakdown of the BOA

$$\Psi_{av} = \Phi_a^{ad} \Theta_{av}^{ad}, \quad \Psi_{bu} = \Phi_b^{ad} \Theta_{bu}^{ad} \qquad (3.34)$$

can be expressed as

$$W_{av} = \frac{2\pi}{\hbar} \sum_u D(E_{bu} - E_{av}) \times \left| \left\langle \Theta_{bu}^{ad} \right| - \sum_i \hbar\omega_i \left\langle \Phi_b^{ad} \left| \frac{\partial}{\partial Q_i} \right| \Phi_a^{ad} \right\rangle \left| \frac{\partial \Theta_{av}^{ad}}{\partial Q_i} \right\rangle \right|^2 \qquad (3.35)$$

where $D(E_{bu} - E_{av})$ denotes the line-shape function. In this case, it could be Lorentzian function

$$D(E_{bu} - E_{av}) = \frac{1}{\pi} \cdot \frac{\Gamma_{bu,av}}{(E_{bu} - E_{av})^2 + \Gamma_{bu,av}^2} \qquad (3.36)$$

where $\Gamma_{bu,av}$ is the broadening parameter. According to eq. (2.6), for the pyrazine case, the molecule is optically pumped from the ground electronic state to the state in the diabatic approximation, in this case we have

$$\left\langle \Phi_2^d \left| \frac{\partial}{\partial Q_c} \right| \Phi_1^d \right\rangle = \frac{\left\langle \Phi_2^d \left| \frac{\partial V}{\partial Q_c} \right| \Phi_1^d \right\rangle}{H_{11} - H_{22}} \qquad (3.37)$$

and to avoid the divergence of eq. (3.37) we change the basic set from (Φ_2^d, Φ_1^d), the "diabatic" approximation, to $(\Phi_2^{ad}, \Phi_1^{ad})$, the adiabatic approximation. Substituting eqs. (3.26) and (3.27) into (3.37) yields

$$\left\langle \Phi_2^d \left| \frac{\partial}{\partial Q_c} \right| \Phi_1^d \right\rangle = \frac{\partial \theta}{\partial Q_c} + \frac{\left\langle \Phi_2^{ad} \left| \frac{\partial V}{\partial Q_c} \right| \Phi_1^{ad} \right\rangle}{U_1 - U_2} \qquad (3.38)$$

According to the eq. (3.30),

$$\frac{\partial \theta}{\partial Q_c} = \frac{\bar{\lambda} \cos^2 2\theta}{H_{11} - H_{22}} = \frac{\bar{\lambda}(H_{11} - H_{22})}{(H_{11} - H_{22})^2 + 4H_{12}^2} \qquad (3.39)$$

For practical calculations, we use the following relation

$$\left\langle \Phi_2^{ad} \left| \frac{\partial V}{\partial Q_c} \right| \Phi_1^{ad} \right\rangle = \cos 2\theta \left\langle \Phi_2^d \left| \frac{\partial V}{\partial Q_c} \right| \Phi_1^d \right\rangle \qquad (3.40)$$

Using the calculated $\pi\pi^*$ and $n\pi^*$ surfaces obtained by Domcke et al, we obtain

$$\left\langle \Phi_2^d \left| \frac{\partial}{\partial Q_c} \right| \Phi_1^d \right\rangle = \frac{2\bar{\lambda}\bar{\kappa}(Q_t - \bar{Q}_t)}{\bar{\kappa}^2 (Q_t - \bar{Q}_t)^2 + 4\bar{\lambda}^2 Q_c^2} \qquad (3.41)$$

The surface properties of the electronic states obtained by Domcke et al are shown in Table 7 and Table 8. The gradients of the excitation energies of the S_1 and S_2 are coming from ref [55], where

$$\kappa_j = \left. \frac{\partial U_j}{\partial Q_t} \right|_0 \qquad (3.42)$$

and

$$\bar{\kappa} = \Delta\kappa = \kappa_2 - \kappa_1 \qquad (3.43)$$

and we assume that

$$\bar{\lambda} = \lambda = \left. \frac{\partial U_j}{\partial Q_c} \right|_0 \qquad (3.44)$$

Then, Huang-Rhys factor S can be obtained from the following formula.

$$S = \frac{1}{2} \left(\frac{\Delta\kappa}{\hbar\omega} \right)^2 \qquad (3.45)$$

Table 7 Harmonic vibrational frequencies (in cm^{-1}) of A_g and B_{1g} normal modes of pyrazine in the electronic ground state from ref [55]. Comparison of MP2 results (DZP basis set) with experiment

	ν_1	ν_2	ν_{6a}	ν_{8a}	ν_{9a}	ν_{10a}
MP2[a]	1 027	3 280	597	1 633	1 264	914
expt.[b]	1 015	3 055	596	1 582	1 230	919

[a] ref [54]

[b] ref [59]

Table 8 Gradients of the excitation energies of the S_1 and S_2 states of pyrazine with respect to the totally symmetric normal coordinates defined at the reference geometry in MRCI method, from ref [55]. S is Huang-Rhys factor

	Q_1	Q_2	Q_{6a}	Q_{8a}	Q_{9a}
$\kappa^{(1)}$ (eV)	-0.0470	0.0368	-0.0964	-0.0623	0.1594
$\kappa^{(2)}$ (eV)	-0.2012	0.0211	0.1193	0.0348	0.0484
$\Delta\kappa$ (eV)	-0.1542	-0.0157	0.2157	0.0971	0.2078
S	0.7333	0.0008	4.2461	0.1150	0.2508

The vibronic coupling constant λ_{10a} is set to 1 472 cm^{-1} in MRCI method. We then obtain the Q-dependent non-adiabatic coupling IC rate as

$$W_{a0} = \pi\hbar\omega_c^2 \sum_{u_t} \sum_{\{u_j\}} D(E_{a0} - E_{bu}) \times \left| \left\langle \chi_{bu_t}\chi_{b1_c} \left| \frac{(Q_t - \bar{Q}_t)}{A_t(Q_t - \bar{Q}_t)^2 + A_c Q_c^2} \right| \chi_{a0_t}\chi_{a0_c} \right\rangle \right|^2 \times \prod_{j(\neq t,c)} |\langle \chi_{bu_j} | \chi_{a0_j} \rangle|^2 \quad (3.46)$$

where

$$A_t \equiv \frac{\Delta\kappa}{2\lambda}, \quad A_c \equiv \frac{2\lambda}{\Delta\kappa} = A_t^{-1} \quad (3.47)$$

In the Condon approximation, the Q-independent non-adiabatic coupling IC rate is

$$W_{a0} = \pi\hbar\omega_c^2 \left| \frac{\lambda}{E_{Vert}} \right|^2 \times \sum_{\{u_j\}} \prod_{j(\neq c)} |\langle \chi_{bu_j} | \chi_{a0_j} \rangle|^2 \delta(E_{a0} - E_{bu}) \quad (3.48)$$

We can define I_{u_t} and $I_{u_t}^{CI}$ to compare the difference between the Franck-Condon factor without and with conical intersection.

$$I_{u_t} \equiv |\langle \chi_{bu_t} | \chi_{a0_t} \rangle|^2 \quad (3.49)$$

$$I_{u_t}^{CI} \equiv \left| \frac{E_{Vert}}{\lambda} \left\langle \chi_{bu_t}\chi_{b1_c} \left| \frac{(Q_t - \bar{Q}_t)}{A_t(Q_t - \bar{Q}_t)^2 + A_c Q_c^2} \right| \chi_{a0_t}\chi_{a1_c} \right\rangle \right|^2 \quad (3.50)$$

It should be noted that the IC lifetime should depend on the line-shape function (see (3.35)). The non-radiative lifetime versus broadening parameter Γ (see eq. (3.35) and (3.36)) have been plotted in Fig. 11. The vertical excited energy changes from 0.50 eV to 1.00 eV. In Fig. 11, it shows that when the vertical excited energies are 0.50 eV or 0.70 eV, and when the broadening parameter Γ tends to 0, the lifetime tends to about 50 fs. From Fig. 11 we can see that the non-adiabatic transition rates depend on Γ and the energy gap.

The purpose of this subsection is to show the treatment of IC with CI. Suzuki et al have employed

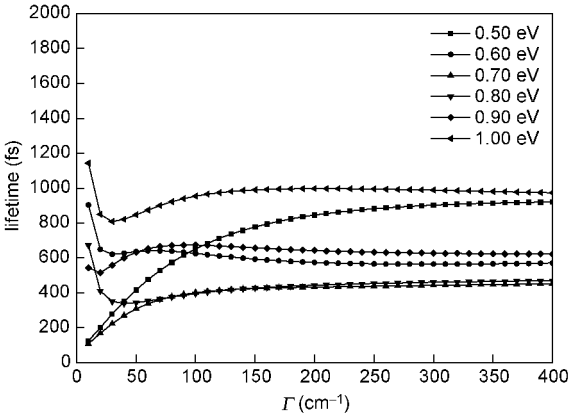

Fig. 11 Lifetime of S_2 state of pyrazine versus broadening parameter Γ, with different vertical excitation energy from 0.50 eV to 1.00 eV

the 22 fs laser pulse for pumping in their studies of the $\pi\pi^* \rightarrow n\pi^*$ dynamics of pyrazine [57]. Suzuki et al used Domcke's model and considered only one $n\pi^*$ PES. However recently we have shown that in pyrazine there are two $n\pi^*$ states lower than $\pi\pi^*$ state [60]. The second $n\pi^*$ state may play an important role in the internal conversion process of $\pi\pi^* \rightarrow n\pi^*$ transition, and affect the lifetime of $\pi\pi^*$ state.

3.4 Vibrational relaxation

3.4.1 Adiabatic approximation

The vibrational relaxation (VR) has been studied for several decades because of its important role in photophysics and photochemistry, especially for the intramolecular vibrational relaxation (IVR), which is the first energy dissipation step of large polyatomic molecules [61—63]. In this section we will show how to study the VR in adiabatic approximation. We will first describe the problem associated with the HOA of molecular vibration. In the HOA, we have

$$T = \sum_i \frac{1}{2}\dot{Q}_i^2, \quad U = \sum_i \frac{1}{2}\omega_i^2 Q_i^2, \quad E = T + U \quad (3.51)$$

and

$$\frac{dE}{dt} = \sum_i \dot{Q}_i(\ddot{Q}_i + \omega_i^2 Q_i) = 0 \qquad (3.52)$$

This indicates that the energy conservation holds for each individual mode. That is, in the harmonic approximation energy exchange between different normal modes is impossible. Taking the anharmonic coupling into account, the anharmonic potential function can be expressed as

$$U = \sum_i \frac{1}{2!}\left(\frac{\partial^2 U}{\partial Q_i^2}\right)_0 Q_i^2 + \sum_{ijk} \frac{1}{3!}\left(\frac{\partial^3 U}{\partial Q_i \partial Q_j \partial Q_k}\right)_0 Q_i Q_j Q_k + \cdots \qquad (3.53)$$

Cross terms can lead to energy flow from one mode to another.

Recently developments in quantum chemical calculations have made it possible to perform the calculations of the anharmonic PES expressed in the form of eq. (3.53) for polyatomic molecule[64]. The anharmonic potential can modify the energy level spacing, produce a maximum quantum number for a vibrational mode and introduce mode-mode coupling. These make the IR spectra exhibit not only fundamental transition bands, but also overtone and combination bands, side bands and often new bands.

In next step we will consider the solution of the Schrödinger equation of vibrational motion with the anharmonic surfaces

$$\hat{H}\Psi = E\Psi \qquad (3.54)$$

where

$$\hat{H} = \hat{T}_Q + \hat{T}_q + V(q, Q) \qquad (3.55)$$

and

$$\hat{T}_Q = -\sum_n \frac{\hbar^2}{2}\frac{\partial^2}{\partial Q_n^2} \qquad (3.56)$$

$$\hat{T}_q = -\sum_i \frac{\hbar^2}{2}\frac{\partial^2}{\partial q_i^2} \qquad (3.57)$$

$$V(Q, q) = V_{\mathrm{H}}(Q) + V_{\mathrm{L}}(q) + V_{\mathrm{int}}(Q, q) \qquad (3.58)$$

$$V_{\mathrm{H}}(Q) = \sum_I \frac{1}{2}\omega_I^2 Q_I^2 + \sum_{IJK} \bar{V}_{IJK} Q_I Q_J Q_K + \sum_{IJKL} \bar{V}_{IJKL} Q_I Q_J Q_K Q_L + \cdots \qquad (3.59)$$

$$V_{\mathrm{L}}(q) = \sum_i \frac{1}{2}\omega_i^2 q_i^2 + \sum_{ijk} \bar{V}_{ijk} q_i q_j q_k + \sum_{ijkl} \bar{V}_{ijkl} q_i q_j q_k q_l + \cdots \qquad (3.60)$$

$$V_{\mathrm{int}}(Q, q) = \sum_{IJi} \bar{V}_{IJi} Q_I Q_J q_i + \sum_{Iij} \bar{V}_{Iij} Q_I q_i q_j + \sum_{Iijk} \bar{V}_{Iijk} Q_I q_i q_j q_k + \sum_{IJij} \bar{V}_{IJij} Q_I Q_J q_i q_j + \sum_{IJKi} \bar{V}_{IJKi} Q_I Q_J Q_K q_i + \cdots \qquad (3.61)$$

Here, the normal modes have been divided into two systems: fast system V_{H} (high frequency modes) and slow system V_{L} (low frequency modes). The fast system evolves adiabatically respected to the slow system without the interaction V_{int}. The energy of fast system will relax to the slow system due to the existence of interaction V_{int}, just as the energy relaxation from electrons to the nuclei in the IC process. Then the formalism of IC process can be used in the VR process.

$\bar{V}$ in (3.59)—(3.61) are the anharmonic expansion coefficients of the PES. In eq. (3.61) for example

$$V_{IJi} \equiv \left(\frac{\partial^3 V}{\partial Q_I \partial Q_J \partial q_i}\right)_0 \qquad (3.62)$$

$$\bar{V}_{IJi} \equiv \frac{1}{3!} V_{IJi} \qquad (3.63)$$

In the BOA, the IC $a \rightarrow b$ can be expressed as

$$W_i = \frac{2\pi}{\hbar}\sum_u \sum_v P_{av} D(E_{av} - E_{bu}) \times \left| \left\langle \Theta_{bu} \right| - \hbar^2 \left\langle \Phi_b \right| \frac{\partial}{\partial Q_i} \left| \Phi_a \right\rangle \left| \frac{\partial \Theta_{av}}{\partial Q_i} \right\rangle \right|^2 \qquad (3.64)$$

$$W = \sum_i W_i \qquad (3.65)$$

$$\left\langle \Phi_b \left| \frac{\partial}{\partial Q_i} \right| \Phi_a \right\rangle = \frac{\left\langle \Phi_b \left| \frac{\partial V}{\partial Q_i} \right| \Phi_a \right\rangle}{U_a(Q) - U_b(Q)} \qquad (3.66)$$

For vibrational relaxation in the adiabatic approximation, the above equation can be used by changing (a, b) into the vibrational quantum numbers of high frequency modes and by changing (u, v) into the quantum numbers of low frequency modes. For example:

$$\frac{\partial V}{\partial q_k} = 6\sum_l \bar{V}_{Ilk} Q_I q_l + \cdots = \sum_l V_{Ilk} Q_I q_l + \cdots \qquad (3.67)$$

We consider the relaxation of Q_I-mode. Notice that $\{q_l\}$ consists of the promoting modes and the accepting modes. The displacement of low frequency

mode q_j comes from the anharmonic coupling term $\bar{V}_{Ij}$ in first-order perturbation theory,

$$U_{N_I}(q_j) = \frac{1}{2}\omega_j^2 q_j^2 + \langle N_I | 3\bar{V}_{Ij} Q_I^2 q_j | N_I \rangle \equiv \frac{1}{2}\omega_j^2 [q_j + d_j(N_I)]^2 + \cdots \quad (3.68)$$

where

$$d_{nj}(N_I) = \frac{3\bar{V}_{Ij}\left(N_I + \frac{1}{2}\right)\hbar}{\omega_j^2 \omega_I} \quad (3.69)$$

represents the displacement of mode j for the specific vibrational state $|N_I\rangle$ of high frequency mode. Then we define the displacement between $|1_I\rangle$ and $|0_I\rangle$ as

$$\Delta d_{Ij} \equiv d_{Ij}(1) - d_{Ij}(0) = \frac{3\bar{V}_{Ij}\hbar}{\omega_j^2 \omega_I} \quad (3.70)$$

and the corresponding Huang-Rhys factor is

$$S_{Ij} = \frac{\omega_I}{2\hbar}\Delta d_{Ij}^2 \quad (3.71)$$

Similar to IC, the vibrational relaxation rate formula can be expressed as

$$W_{Ik}^{a0} = \frac{\omega_I^2}{4} R_{Ik}^2 \int_{-\infty}^{\infty} dt \times \exp\left\{ it(\omega_I - \omega_i - \omega_k) - \sum_{j(\neq I,k)} S_{Ij}(1 - e^{-it\omega_j}) \right\} \quad (3.72)$$

and the total decay rate is given by

$$W_I^0 = \sum_{i \leqslant k} W_{Ik}^{a0} \quad (3.73)$$

where

$$R_{Ik} = \frac{V_{Ik}}{\hbar\omega_I} \quad (3.74)$$

and

$$V_{Ik} = \frac{\partial^3 V}{\partial Q_I \partial q_I \partial q_k}\sqrt{\frac{\hbar^3}{\omega_I \omega_i \omega_k}} \quad (3.75)$$

3.4.2 Vibrational relaxation of water dimer

As an example to apply the adiabatic approximation theory of VR, the hydrogen-bonded water dimer $(H_2O)_2$ will be studied in this work. The structure of $(H_2O)_2$ was optimized using Gaussian 09 program[65] with DFT method and CAM-B3LYP / 6-311 + + g(d, p) long range corrected version of B3LYP functional[66]. The point group of water dimer is C_S. There are 8 symmetric modes and 4 antisymmetric modes. The frequencies have been listed in Table 9.

Table 9 The symmetries and frequencies of normal modes of water dimer

	v_1	v_2	v_3	v_4	v_5	v_6	v_7	v_8	v_9	v_{10}	v_{11}	v_{12}
symmetry	a″	a′	a″	a′	a′	a″	a′	a′	a′	a′	a′	a″
freq. (cm^{-1})	138	165	175	206	374	692	1 606	1 623	3 739	3 853	3 932	3 951

Employing eq. (3.71), Huang-Rhys factors S_{Ij} can be calculated and listed in Table 10. The Huang-Rhys factor is related with mode displacement in eq. (3.69), which is determined by the anharmonic expansion coefficient V_{Ij}. I and j are the indexes of high frequency mode and low frequency mode respectively. According to group theory, V_{Ij} with antisymmetric low frequency mode j is vanished. This means that only symmetric low frequency mode can contribute to the Huang-Rhys factor, which can be obviously observed in Table 10.

Overall vibrational relaxation rates for modes 7—12 are calculated according to eq. (3.73) and listed in Table 11. From these tables, we can see that the fastest vibrational relaxation rate is $1.93 \times 10^{10}\ s^{-1}$ for the mode 9. This is consistent with the experimental data of Miller et al[67] estimating from the spectral band-width.

Table 10 Huang-Rhys factors of water dimer in adiabatic approximation

	$S_{7j}(\times 10^{-3})$	$S_{8j}(\times 10^{-3})$	$S_{9j}(\times 10^{-3})$	$S_{10j}(\times 10^{-3})$	$S_{11j}(\times 10^{-3})$	$S_{12j}(\times 10^{-3})$
1	0	0	0	0	0	0
2	0.0085	1.7311	10.2435	0.4038	0.3522	1.0797
3	0	0	0	0	0	0
4	0.1028	0.3378	0.3926	0.0375	0.0079	0.1278
5	0.6162	1.9333	0.3049	0.2603	0.6763	0.5117
6	0	0	0	0	0	0
7			0.1604	0.0590	0.7028	1.6853
8			0.0191	0.0169	1.1456	0.8310

Table 11 The overall vibrational relaxation rate

mode	freq. (cm^{-1})	rate (s^{-1})	lifetime (ps)
7	1 606	2.24×10^{9}	446
8	1 623	4.53×10^{7}	22 079
9	3 739	1.93×10^{10}	52
10	3 853	4.15×10^{9}	241
11	3 932	2.80×10^{9}	357
12	3 951	7.94×10^{8}	1 259

Regarding the VR in liquid water, in view of the fact that the "ice water" is believed to play a very important role in liquid water and contains important well-defined water clusters of size four and five, the vibrational relaxation of these water clusters will be studied in the future.

3.4.3 Intramolecular vibrational relaxation of aniline

The IVR of the NH_2 symmetric and asymmetric stretching vibrations of jet-cooled aniline has been investigated by picosecond time-resolved IR-UV pump-probe spectroscopy [68, 69]. The frequency of asymmetric stretching vibration mode (v_a) 3 509 cm^{-1} is a little higher than that of symmetric stretching vibration mode (v_s) 3 423 cm^{-1} [70]. In the picosecond pump-probe experiment, the IVR of the NH_2 stretching modes are described by two-step tier model. The symmetric or asymmetric stretching mode is initially excited to the vibrational excited state. In the first step, the energy flows into the doorway states [71, 72], and secondly the energy is further redistributed to dense base states. By fitting the transient (1 + 1) REMPI spectra of aniline, the IVR rates of NH_2 symmetry and asymmetric stretching vibrations are summarized as follows [69].

(1) v_s(3 423 cm^{-1}) ,

$k_1 = 5.6 \times 10^{10}\ s^{-1}$, $k_2 = (0.1—5) \times 10^{10}\ s^{-1}$

(2) v_a(3 509 cm^{-1}) ,

$k_1 = 2.9 \times 10^{10}\ s^{-1}$, $k_2 = (0.1—2) \times 10^{10}\ s^{-1}$

In this subsection, we calculate the IVR rates of NH_2 symmetry and asymmetry stretching vibrations of aniline, and compare the results with k_1.

The structure of aniline was optimized using Gaussian 09 program [65] with DFT method and B3LYP / 6-311 + + g(d,p) .

Table 12 and Table 13 list the vibrational relaxation paths for symmetry and asymmetry stretching vibration modes, which IVR rates are larger than $1 \times 10^{9}\ s^{-1}$. The theoretical results of IVR rates, $v_s = 10.11 \times 10^{10}\ s^{-1}$ and $v_a = 1.59 \times 10^{10}\ s^{-1}$, are as the same orders of magnitude as the experimental values. It also shows that the IVR rate of symmetry mode is larger than that of asymmetry mode. Due to selection rule, the NH_2 scissoring and C—C stretching symmetry modes 28 and 29 can accept relaxation energy from symmetry mode 35 at the same time. This makes that the accepting energy for symmetry mode 35 be smaller than that for asymmetry mode 36, then enhance the IVR rate according to energy gap law.

Table 12 Vibrational relaxation paths for symmetry stretching mode of NH_2(mode 35)

I	l	k	R_{nlk}	accpt. energy (cm^{-1})	rate (s^{-1})
35	29	29	0.010	242	8.24×10^{10}
35	29	28	0.005	261	1.58×10^{10}
35	28	28	0.002	281	0.24×10^{10}
total					10.11×10^{10}

Table 13 Vibrational relaxation paths for asymmetry stretching mode of NH_2(mode 36)

I	l	k	R_{nlk}	accpt. energy (cm^{-1})	rate (s^{-1})
36	29	18	0.012	939	0.26×10^{10}
36	29	19	-0.009	869	0.24×10^{10}
36	29	27	-0.002	377	0.18×10^{10}
36	29	25	0.003	504	0.18×10^{10}
36	29	24	0.004	636	0.14×10^{10}
36	28	18	0.006	958	0.13×10^{10}
36	28	19	-0.005	888	0.12×10^{10}
total					1.59×10^{10}

It should be noted that our attempt to calculate VR rate for clusters and complex systems should be regarded as a preliminary attempt because the anharmonic PESs themselves are approximate and their performance should be carefully examined by calculating IR spectra and compared with the experiments.

4 Conclusions

In this paper, we have introduced recent developments of radiationless transitions, anharmonic effects on photophysical processes, internal conversion and vibrational relaxation processes. For the molecule formaldehyde, the PES of second electronic excited state appears double well shape. Due to the selection

rule, the absorption from $S_0(^1A_1) \rightarrow S_1(^1A_2)$, and emission from $S_1(^1A_2) \rightarrow S_0(^1A_1)$ are symmetry forbidden. The spectra intensity can be regarded as borrowing through vibronic coupling with other electronic states. The Q-dependent electronic wavefunction can be obtained perturbatively. Then the electronic transition dipole moment and nonadiabatic coupling are calculated directly. The double well potential is fitting to the sum of harmonic potential function and Gaussian function, and then the Franck-Condon factors can be simplified to harmonic cases.

The second case is about the theory of absorption, emission spectra and IC rate about anharmonic PES (see eq. (3.3)). Actually, the PES in this case can be a general form of Taylor expansion respected to normal coordinate Q according to eq. (3.2). The cumulant expansion is used to derive the thermal correlation functions. The anharmonic effects are reflected in the modifications of the energy difference ω_{ba} and the Huang-Rhys factor S_j. As applications, the absorption, emission spectra of pyridine, pyrimidine and fluorobenzene, and the IC rate of fluorobenzene were calculated. The results are in a good agreement with the experiments.

The third case is about the method to calculate the IC with CI. We have proposed one method to calculate the IC rate of $\pi\pi^* \rightarrow n\pi^*$ of the pyrazine molecule. The pump-probe experimental measurement of its $\pi\pi^*$ state lifetime is determined to be ~ 22 fs by Suzuki et al. They employed the PESs model from Domcke [56] to obtain the lifetime of $S_2(\pi\pi^*)$. It should be noted that in pyrazine, there should exist two $n\pi^*$ states. But they only include one $n\pi^*$ state in their treatments of non-adiabatic processes. In a very recent paper we have studied this neglected $n\pi^*$ surface and studied its effect on the experimental spectra [60]. The work in progress is to calculate the lifetime of $\pi\pi^*$ state by using the new set of PESs of pyrazine.

The fourth case is about the theoretical studies of VR, which can be applied to that in isolated molecules, molecular cluster and dense media. This type of PES has become available in recent quantum chemistry programs. Although theories of VR have been proposed, its numerical calculations have only become possible recently. The VR under consideration depends on the size of the system and takes place in the time range of sub-picoseconds to picoseconds. In this paper we have chosen the water dimer and aniline as the systems for investigations. The PES includes the harmonic, cubic anharmonic contributions. Applying the adiabatic approximation, the normal modes can be divided into fast system (high frequency modes) and slow system (low frequency modes). The energy of fast system can relax to the slow system due to the existence of the interaction between these two systems (anharmonic couplings between high frequency modes and low frequency modes). Then the formalism of IC process can be used to derive the VR rate from high frequency modes to the low frequency modes. Thus concepts of "promoting" modes and "accepting" modes also exist in the formalism of VR. In this paper, we only apply the first order perturbation theory to deal with the interaction term V_{int} in the adiabatic approximation. This will be improved in the future.

Reference

[1] Lin S H. J. Chem. Phys., 1966, 44(10): 3759—3767

[2] Englman R, Jortner J. Mol. Phys., 1970, 18(2): 145—164

[3] Freed K F, Jortner J. J. Chem. Phys., 1970, 52(12): 6272—6291

[4] Nitzan A, Jortner J. J. Chem. Phys., 1971, 55(3): 1355—1368

[5] Siebrand W. J. Chem. Phys., 1971, 54(1): 363—367

[6] Fischer S. Chem. Phys. Lett., 1971, 11(5): 577—582

[7] Lin S H, Bersohn R. J. Chem. Phys., 1968, 48(6): 2732—2736

[8] Henry B R, Kasha M. Annu. Rev. Phys. Chem., 1968, 19(1): 161—192

[9] Huang K, Rhys A. Proc. R. Soc. Lond. A, 1950, 204: 406—423

[10] Huang K. Contemp. Phys., 1981, 22(6): 599—612

[11] Duschinsky F. Acta Physicochim. (USSR), 1937, 7: 551—566

[12] Hayashi M, Mebel A M, Liang K K, Lin S H. J. Chem. Phys., 1998, 108(5): 2044—2055

[13] Mebel A M, Hayashi M, Liang K K, Lin S H. J. Phys. Chem. A, 1999, 103(50): 10674—10690

[14] Peng Q, Yi Y, Shuai Z, Shao J. J. Chem. Phys., 2007, 126: art. no. 114302

[15] Peng Q, Yi Y, Shuai Z, Shao J. J. Am. Chem. Soc., 2007, 129: 9333—9339

[16] Niu Y, Peng Q, Shuai Z. Sci. China Ser. B-Chem., 2008, 51

(12): 1153—1158

[17] Tang J, Lee M T, Lin S H. J. Chem. Phys., 2003, 119(14): 7188—7196

[18] Islampour R, Miralinaghi M. J. Phys. Chem. A, 2007, 111(38): 9454—9462

[19] Islampour R, Miralinaghi M. J. Phys. Chem. A, 2009, 113(11): 2340—2349

[20] Pople J A, Sidman J W. J. Chem. Phys., 1957, 27(6): 1270—1277

[21] Robinson G W, Digiorgio V E. Can. J. Chem., 1958, 36(1): 31—38

[22] Callomon J H, Innes K K. J. Mol. Spectrosc., 1963, 10(1/6): 166—181

[23] Job V A, Sethuraman V, Innes K K. J. Mol. Spectrosc., 1969, 30(1/3): 365—426

[24] Moule D C, Walsh A D. Chem. Rev., 1975, 75(1): 67—84

[25] Miller R G, Lee E K C. J. Chem. Phys., 1978, 68(10): 4448—4464

[26] Strickler S J, Barnhart R J. J. Phys. Chem., 1982, 86(4): 448—455

[27] Jensen P, Bunker P R. J. Mol. Spectrosc., 1982, 94(1): 114—125

[28] Clouthier D J, Ramsay D A. Ann. Rev. Phys. Chem., 1983, 34(1): 31—58

[29] Reisner D E, Field R W, Kinsey J L, Dai H. J. Chem. Phys., 1984, 80(12): 5968—5978

[30] Lin C K, Chang H C, Lin S H. J. Phys. Chem. A, 2007, 111(38): 9347—9354

[31] Coon J B, Naugle N W, Mckenzie R D. J. Mol. Spectrosc., 1966, 20(2): 107—129

[32] Lin S H, Eyring H. Proc. Nat. Acad. Sci. USA, 1974, 71(9): 3415—3417

[33] Lin S H. Proc. R. Soc. Lond. A, 1976, 352(1668): 57—71

[34] Lin S H, Fujimura Y, Neusser H J, Schlag E W. Multiphoton Spectroscopy of Molecules. New York: Academic Press, 1984

[35] Yeung E S, Moore C B. J. Chem. Phys., 1973, 58(9): 3988—3998

[36] Miller R G, Lee E K C. Chem. Phys. Lett., 1975, 33(1): 104—107

[37] Miller R G, Lee E K C. Chem. Phys. Lett., 1976, 41(1): 52—54

[38] Yeung E S, Moore C B. J. Chem. Phys., 1974, 60(5): 2139—2147

[39] Tang K Y, Fairchild P W, Lee E K C. J. Chem. Phys., 1977, 66(7): 3303—3305

[40] Liang K K, Chang R, Hayashi M, Lin S H. Principle of Molecular Spectroscopy and Photochemistry. Taichung: National Chung Hsing University Press, 2001

[41] Lin C, Li M, Yamaki M, Hayashi M, Lin S H. Phys. Chem. Chem. Phys., 2010, 12(37): 11432—11444

[42] Zhu C, Liang K K, Hayashi M, Lin S H. Chem. Phys., 2009, 358(1/2): 137—146

[43] Wang H, Zhu C, Yu J, Lin S H. J. Phys. Chem. A, 2009, 113(52): 14407—14414

[44] Villa E, Amirav A, Lim E C. J. Phys. Chem., 1988, 92(19): 5393—5397

[45] Mochizuki Y, Kaya K, Ito M. J. Chem. Phys., 1978, 69(2): 935—936

[46] Yang L, Zhu C Y, Yu J G, Lin S H. Chem. Phys., doi: 10.1016/j.chemphys.2012.03.010

[47] Da Silva F F, Almeida D, Martins G, Milosavljevic A R, Marinkovic B P, Hoffmann S V, Mason N J, Nunes Y, Garcia G, Limao-Vieira P. Phys. Chem. Chem. Phys., 2010, 12(25): 6717—6731

[48] Knight A E W, Lawburgh C M, Parmenter C S. J. Chem. Phys., 1975, 63(10): 4336—4351

[49] Butler P, Moss D B, Yin H, Schmidt T W, Kable S H. J. Chem. Phys., 2007, 127(9): art. no. 94303

[50] Lin S H. J. Chem. Phys., 1973, 58(12): 5760—5768

[51] Werner H J, Knowles P J, Lindh R, Manby F R, Celani P, Korona T, Rauhut G, Amos R D, Bernhardsson A, Berning A, Cooper D L, Dobbyn A J, Eckert F, Hampel C, Hetzer G, Lloyd A W, Mcnicholas S J, Meyer W, Mura M E, Nicklaβ A, Palmieri P, Pitzer R, Schumann U, Stoll H, Tarroni R, Thorsteinsson T. Molpro. 2006

[52] Abramson A S, Spears K G, Rice S A. J. Chem. Phys., 1972, 56(5): 2291—2308

[53] He R X, Yang L, Zhu C Y, Yamaki M, Lee Y P, Lin S H. J. Chem. Phys., 2011, 134(9): art. no. 94313

[54] Seidner L, Stock G, Sobolewski A L, Domcke W. J. Chem. Phys., 1992, 96(7): 5298—5309

[55] Woywod C, Domcke W, Sobolewski A L, Werner H. J. Chem. Phys., 1994, 100(2): 1400—1413

[56] Seel M, Domcke W. J. Chem. Phys., 1991, 95(11): 7806—7822

[57] Suzuki Y, Fuji T, Horio T, Suzuki T. J. Chem. Phys., 2010, 132(17): art. no. 174302

[58] Werner U, Mitric R, Suzuki T, Bonacic-Kouteck V. Chem. Phys., 2008, 349(1/3): 319—324

[59] Innes K K, Ross I G, Moomaw W R. J. Mol. Spectrosc., 1988, 132(2): 492—544

[60] Lin C K, Niu Y L, Zhu C Y, Shuai Z G, Lin S H. Chem. Asian J., 2011, 6(11): 2977—2985

[61] Laubereau A, Kaiser W. Rev. Mod. Phys., 1978, 50(3): 607—665

[62] Nesbitt D J, Field R W. J. Phys. Chem., 1996, 100(31): 12735—12756

[63] Voth G A, Hochstrasser R M. J. Phys. Chem., 1996, 100(31): 13034—13049

[64] Barone V. J. Chem. Phys., 2005, 122(1): art. no. 14108

[65] Frisch M J, Trucks G W, Schlegel H B, Scuseria G E, Robb M A, Cheeseman J R, Scalmani G, Barone V, Mennucci B, Petersson G A, Nakatsuji H, Caricato M, Li X, Hratchian H P, Izmaylov A F, Bloino J, Zheng G, Sonnenberg J L, Hada M,

Ehara M, Toyota K, Fukuda R, Hasegawa J, Ishida M, Nakajima T, Honda Y, Kitao O, Nakai H, Vreven T, Montgomery J J A, Peralta J E, Ogliaro F, Bearpark M, Heyd J J, Brothers E, Kudin K N, Staroverov V N, Kobayashi R, Normand J, Raghavachari K, Rendell A, Burant J C, Iyengar S S, Tomasi J, Cossi M, Rega N, Millam N J, Klene M, Knox J E, Cross J B, Bakken V, Adamo C, Jaramillo J, Gomperts R, Stratmann R E, Yazyev O, Austin A J, Cammi R, Pomelli C, Ochterski J W, Martin R L, Morokuma K, Zakrzewski V G, Voth G A, Salvador P, Dannenberg J J, Dapprich S, Daniels A D, Farkas Ö, Foresman J B, Ortiz J V, Cioslowski J, Fox D J. Gaussian 09. Gaussian, Inc.

[66] Yanai T, Tew D P, Handy N C. Chem. Phys. Lett., 2004, 393(1/3): 51—57

[67] Huang Z S, Miller R E. J. Chem. Phys., 1989, 91(11): 6613—6631

[68] Yamada Y, Okano J, Mikami N, Ebata T. Chem. Phys. Lett., 2006, 432(4/6): 421—425

[69] Yamada Y, Okano J, Mikami N, Ebata T. J. Chem. Phys., 2005, 123(12): art. no. 124316

[70] Ebata T, Minejima C, Mikami N. J. Phys. Chem. A, 2002, 106(46): 11070—11074

[71] Hutchinson J S, Reinhardt W P, Hynes J T. J. Chem. Phys., 1983, 79(9): 4247—4260

[72] Ebata T, Kayano M, Sato S, Mikami N. J. Phys. Chem. A, 2001, 105(38): 8623—8628

《化学进展》近期目次预告

黄鸣龙——我国有机化学的一位先驱(韩广甸　金善炜　吴毓林)

离子液体的定量结构-性质/活性研究(赵永升　张香平　赵继红　张宏忠　康雪晶　董 峰)

CO 催化氧化用纳米材料及其最新研究进展(张俊　陈婧　黄新松　李广社)

分子筛在加氢脱硫催化剂深度脱硫方面的应用(尹海亮　周同娜　柴永明　柳云骐　刘晨光)

核壳型沸石复合材料和反应器(陈立峰　史静　张亚红　唐 颐)

磁性有序介孔炭的合成及新应用(田勇　王加　钟国英　林汉森　王秀芳)

碲化镉纳米晶的制备及应用进展(赵冬梅　孙立国　王彦杰　杜宇虹　汪成)

多肽在贵金属纳米粒子制备中的应用(陶凯　王继乾　夏道宏　徐 海　吕建仁　山红红)

POMSS 配位化合物(李昂　张春玲　孙国恩　牟建新)

基于钯催化 C—H 键活化的多米诺反应(沈金海　程国林　崔秀灵)

双分子层膜人工离子通道的合成与研究进展(包春燕　贾慧娟　刘涛　汪奕　彭伟　朱麟勇)

蛋氨酸亚砜还原酶及其在白内障发生发展中的作用(李轶　李琳　黄开勋)

自修复高分子材料(李思超　韩朋　许华平)

基于聚环氧乙烷链和亚苯基的刚棒-线团分子自组装(钟克利　陈铁　金龙一)

聚合物发光电化学池(张驰　刘治田　沈陟　刘菁)

双环戊二烯反应注塑(曹堃　付强　周立武　姚臻)

天然水体中可溶性有机质的自由基光化学行为(郜超　李雁宾　阴永光　蔡勇　江桂斌)

面向食品安全分析的核酸适配体传感技术(梁淼　刘锐　苏荣欣　齐崴　王利兵　何志敏)

离子液体支撑液膜分离 CO_2(段永超　伍艳辉　于世昆　李佟茗)

微藻高油脂化基因工程研究策略(冯国栋　程丽华　徐新华　张林　陈欢林)